TESTING AND EVALUATION OF THE DEFORMATION EFFECTS DEVELOPED BY LANDSLIDES IN THE LABORATORY WITH IMAGE PROCESSING TECHNIQUES

HEYELANLARIN YARATMIŞ OLDUĞU DEFORMASYON ETKİLERİNİN GÖRÜNTÜ İŞLEME YÖNTEMLERİYLE LABORATUVARDA TEST EDİLMESİ VE DEĞERLENDİRİLMESİ

ABDULLAH ENES ÖZŞİMŞİR

ASSOC. PROF. DR. MUSTAFA KEREM KOÇKAR
Supervisor

Submitted to
Graduate School of Science and Engineering of Hacettepe University
as a Partial Fulfilment to the Requirements
for the Award of the Degree of Master of Science
in Civil Engineering.

2024

ABSTRACT

TESTING AND EVALUATION OF THE DEFORMATION EFFECTS DEVELOPED BY LANDSLIDES IN THE LABORATORY WITH IMAGE PROCESSING TECHNIQUES

Abdullah Enes Özşimşir

Master of Science, Department of Civil Engineering

Supervisor: Assoc. Prof. Dr. Mustafa Kerem Koçkar

January 2024, 94 pages

Landslides are one of the most frequently encountered natural disasters in Türkiye and the world, which can cause significant loss of life and property. Nowadays, various methods such as inclinometers, tiltmeters, extensometers, fiber optic methods, and ground-based surface measurement systems (i.e., LIDAR, electro-optics, total station) are used to monitor sliding mass with potential stability risks. In recent years, image processing techniques have become popular; however, their use in landslide investigations has not yet expanded to the desired level. With the development of image processing techniques, image recordings are used in many sectors for analysis during or after the studies. By this way, real-time data collection and rapid response capabilities can be increased to manage possible disaster situations effectively. This thesis uses image processing methods to detect the deformation movement on the sliding surface caused by any triggering mechanism (i.e., excessive rainfall, earthquake, human factors, sudden snowmelt), regardless of lithological unit and failure types. For this purpose, the deformation movement on an artificial landslide simulator created on a shaking table operating as a triggering mechanism in the laboratory environment was analyzed. The tilt sensor was integrated into the landslide simulator in the vertical direction, and laser measurements were performed to evaluate the accuracy of the results obtained by image processing. This study is a prototype that analyses mass movements from different perspectives in a laboratory environment. It offers new perspectives for monitoring landslides and, accordingly, for natural disaster management and risk reduction strategies.

Keywords: Monitoring of Mass Movements, Image Processing, Landslide Simulator, Shaking Table, Tilt Sensor, Slope Stability

ÖZET

HEYELANLARIN YARATMIŞ OLDUĞU DEFORMASYON ETKİLERİNİN GÖRÜNTÜ İŞLEME YÖNTEMLERİYLE LABORATUVARDA TEST EDİLMESİ VE DEĞERLENDİRİLMESİ

Abdullah Enes ÖZŞİMŞİR

Yüksek Lisans, İnşaat Mühendisliği Bölümü

Tez Danışmanı: Doç. Dr. Mustafa Kerem KOÇKAR

Ocak 2024, 94 sayfa

Heyelanlar hem Türkiye'de hem de dünyada sıklıkla karşılaşılan büyük can ve mal kayıplarına neden olabilecek doğal afetlerden biridir. Günümüzde potansiyel kayma tehlikesi olan kütle hareketlerinin (örneğin, heyelanlar) izlenmesi için inklinometreler, tiltmetreler, ekstensometreler, fiber optik ve yersel yüzeysel ölçüm sistemleri (örneğin, LIDAR, elektro optik, total istasyon, vb.) gibi çeşitli yöntemler kullanılmaktadır. Son yıllarda görüntü işleme teknikleri popüler bir uygulama haline gelmiştir; ancak bu tekniklerin heyelan araştırmalarında kullanım alanı henüz istenilen düzeyde genişlememiştir. Gelişen görüntü işleme teknikleriyle birlikte birçok sektörde görüntü kayıtları yapılan aygıtlar, çalışmalar esnasında veya sonrasında incelemeler yapmak için kullanılmaktadır. Bu şekilde, gerçek zamanlı veri toplama ve hızlı müdahale kabiliyetleri artırılabilir, böylece olası felaket durumlarına daha etkili bir şekilde müdahale edilebilir. Bu tezin amacı litolojik birim ve yenilme tiplerinden bağımsız olarak herhangi bir tetikleme mekanizması (örneğin, aşırı yağış, deprem, beşeri faktörler, ani kar erimesi, vb.) sonucunda oluşan kayma yüzeyindeki deformasyon hareketini görüntü işleme yöntemleriyle tespit edebilmektir. Bu amaçla, laboratuvar ortamında tetikleme mekanizması olarak çalışan bir sarsma tablası üzerinde oluşturulan yapay heyelan simülatörü üzerindeki deformasyon hareketi incelenmiştir. Görüntü işleme ile elde edilen sonuçların doğruluğunun değerlendirilmesi için heyelan simülatörüne düşey yönde hareketi algılayan eğim sensörleri entegre edilmiş ve lazer ölçümleri yapılmıştır. Bu çalışma, laboratuvar ortamında kütle hareketlerini farklı bakış açılarından inceleyen bir prototip niteliğindedir. Heyelanların izlenmesi ve buna bağlı olarak doğal afet yönetimi ve risk azaltma stratejileri açısından ele alınmasına yönelik yeni perspektifler sunmaktadır.

Anahtar Kelimeler: Kütle Hareketlerinin İzlenmesi, Görüntü İşleme, Heyelan Simülatörü, Sarsma Tablası, Eğim Sensörü, Şev Stabilitesi

ACKNOWLEDGEMENTS

First, I would like to express my gratitude to my supervisor, Assoc. Prof. Dr. Mustafa Kerem Koçkar for his guidance, support, valuable advice, and efforts, as well as his understanding, tolerance, and patience during the challenging periods. I cannot thank him enough for making me feel that he was with me at every stage of the study, regardless of the day and time, by providing full support in every matter.

I would like to thank the members of the examining committee, Prof. Dr. Haluk Akgün, Prof. Dr. Berna Unutmaz, Prof. Dr. Mustafa Şahmaran, and Assoc. Prof. Dr. Mustafa Abdullah Sandıkkaya for their valuable criticism and remarks during my thesis defense period.

I would like to thank Furkan Can Yaşar and Damla Anafarta, who helped me in the early stages of my business life and patiently answered all my questions. I always felt their support. I would also like to thank Merve Yüzbaşı, with whom I gained many valuable experiences. I feel fortunate to have worked with this team.

Without my family, I wouldn't have moved forward on this path. I am grateful for their encouragement, support, and guidance during my academic career. Their love and support have been my biggest motivation in every aspect of my life.

I would like to thank the Hacettepe Earthquake Simulation Laboratory team, which I joined by opening a new page in my life. I could not have made this journey without Dr. Arzu Arslan Kelam, Mr. Gökhan Şahin, Mr. Cem Demir, Mr. Ahmet Kaan Karabulut, Mr. Yunus Emre Kaya and Mr. Barış Ural. The creative ideas, hard work, and harmony of this team made things easier for me. I would also like to thank Mustafa Hatipoğlu for his great support in this study. He has made valuable contributions to this study on sensors.

Finally, I would like to express my thanks to The Scientific and Technological Research Council of Türkiye for funding this study performed in the scope of the ARDEB-1001, Grant No: 121M761 research project. I would like to thank the BİDEB department of TÜBİTAK for their support under the BİDEB-2210 program.

Finally, I would like to express my gratitude to the Disaster and Emergency Management Authority (AFAD), Yalova University, Rector Prof. Dr. Mehmet Bahçekapılı and Vice Rector Prof. Dr. Cahit Külekçi for their support.

TABLE OF CONTENTS

LIST OF FIGURES

LIST OF TABLES

1. INTRODUCTION

Natural disasters have been one of the biggest threats faced by humanity from the past to the present. Among these disasters, landslides are one of the most important natural disasters that cause both loss of life and material losses. Monitoring is the movement of landslides; detecting them in advance is critical for preventing or mitigating such disasters.

“Landslides” are natural disasters usually occurring along the sliding mass or inclined terrains. A landslide is a type of mass movement, which implies the downward or outward movement of soil or rocks along a sloping surface. They play an essential role in erosion. Landslides also create deep scars in the topography. Such events can often be triggered by various natural factors such as rainfall, earthquakes, and ice melting. Concerning these natural or environmental factors, erosion, saturation of the ground, penetration of surface water, etc. may occur. Local geological conditions can also influence the probability of landslides.

Three devastating landslides throughout history highlight the deadly potential of these geological events. In 1963, the Monte Toc landslide in Italy triggered a megatsunami and claimed nearly 2,000 lives (Barla & Paronuzzi, 2013). The Thredbo landslide in Australia in 1997 similarly buried a hostel (Sim et al., 2022). In Venezuela's Vargas State in 1999, mudslides caused by heavy rainfall resulted in tens of thousands of fatalities (Carroll, 2014). In January 2011, the 2011 Rio de Janeiro landslide (Figure 1) caused 610 deaths in Rio de Janeiro, Brazil (Alcântara et al., 2023). These remarkable examples reveal the necessity of taking appropriate precautions in landslide-prone areas.

Figure 1. January 2011 Rio de Janeiro floods and mudslides

According to the Fatal Landslide Database of Türkiye (FATALDOT), an average of 4 fatal landslides occur each year in Türkiye, killing an average of 15 people. Landslides were found to be the second most deadly type of natural disaster in Türkiye after earthquakes. Over the last 20 years, there has been a rise in the average occurrence of fatal landslides, reaching 12 %, with the corresponding average number of fatalities increasing to 24 % (Topaçli et al., 2023).

"AFAD carried out Disaster Information Inventory Project" (ABEP) to create a reference source including disaster events that have occurred in Türkiye since the 1950s, to facilitate office and field investigations, to form a primary basis for disaster hazard studies of all types and scales, to make retrospective analyzes of the studies carried out and to reveal the economic and moral damages of disasters. This project shows that the total number of disaster victims affected by landslides is 59,345, with a share of 21 percent in terms of disaster types. Figures 2 and 3 show the distribution of the number of landslide disaster events and the number of disaster victims by provinces in Türkiye, respectively, according to the results obtained from the project (Gürer & Uçar, 2022). In addition, images of the Çatak landslide, a disaster in Trabzon in 1988, in which 64 people lost their lives, are given in Figure 4.

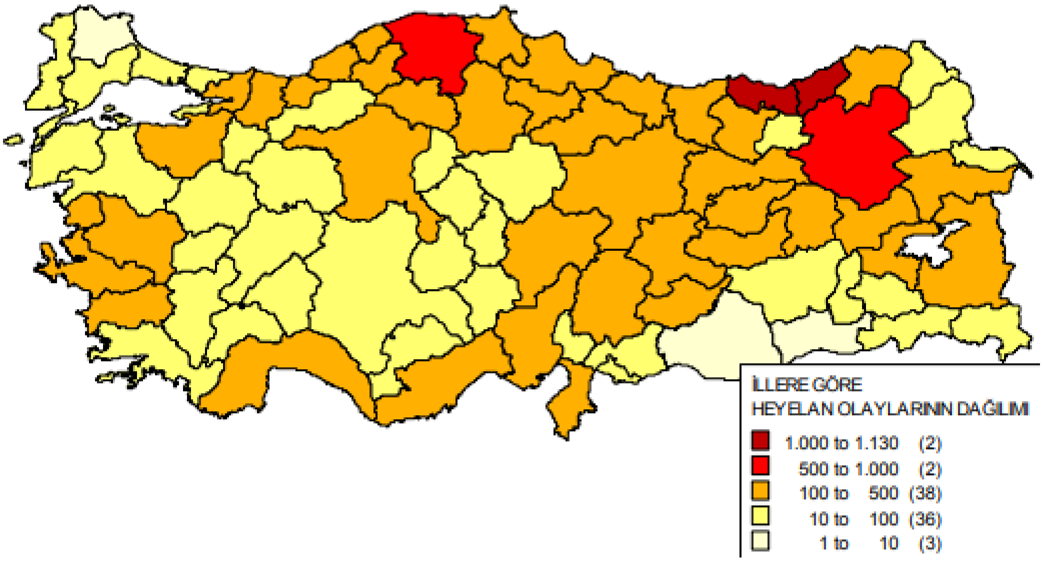

Figure 2. Distribution of the number of landslides by provinces in Türkiye (AFAD,2008)

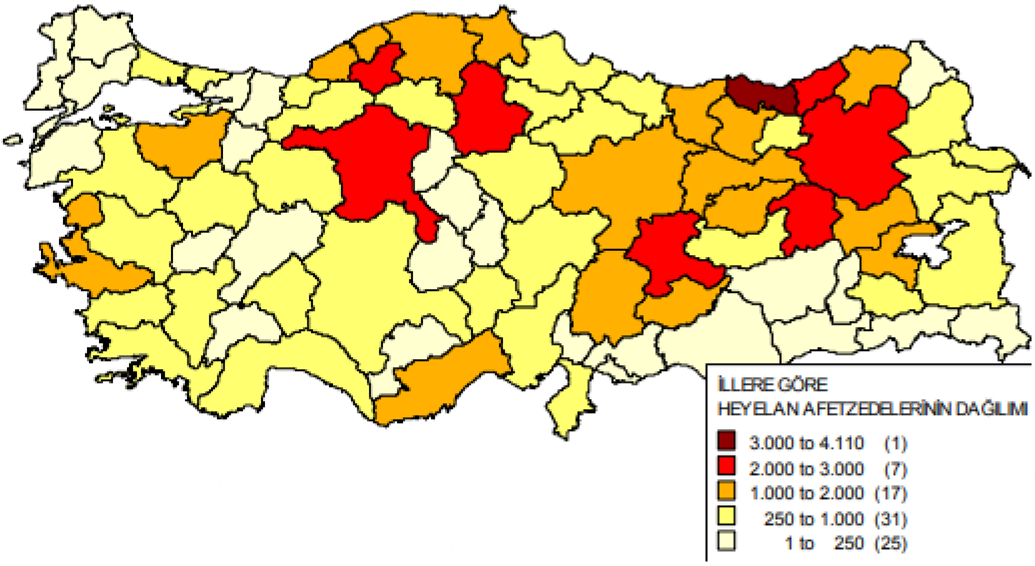

Figure 3. Distribution of landslide disaster victims by provinces in Türkiye (AFAD,2008)

Figure 4. 1988 Trabzon/Çatak Landslide

In recent years, the awareness of landslides and the importance given to the concept of risk management have increased rapidly, and monitoring and early warning systems have received much attention (Liu et al., 2010; Pei et al., 2011; Li et al., 2012; Chae et al., 2017; Ju et al., 2020). Nowadays, there are methods using different equipment to monitor sliding mass or landslides with potential slip hazards. Among this equipment, inclinometers, tiltmeters, extensometers, ground surface measurement systems (i.e., radar, laser scanner, electro-optical, total station), and fiber optic methods are used to monitor landslides and/or unstable slopes (Savvaidis, 2003; Pei et al., 2011).

There are some exemplary studies on this topic using a shaking table to investigate deformation movements on a laboratory scale (Wartman et al., 2005; Lin and Wang, 2006; Lai et al., 2013; Zhao et al., 2015; Srilatha et al., 2016; Edinçliler and Toksoy, 2017; Yin and Wang, 2019). Numerous studies have investigated the dynamic displacement behavior of unstable soils to prevent slope failures triggered by earthquakes and under seismic loads along with the effectiveness of various retaining structures like geosynthetics and soil nails. Papini et al. (2020) delve specifically into analyzing this behavior using fiber optic sensors on laboratory-scale slopes with varying angles. Similarly, Akgün et al. (2021) focus on evaluating the sensitivity of dynamic displacement measurements and their application to mass movements using fiber optic sensors.

In recent years, with the development of image processing techniques, new and effective methods have been developed to monitor and analyze the movement of simulated landslides in a laboratory environment. These methods include algorithms to detect, monitor, and analyze landslide movement from video images. This way, real-time data provision, and rapid response capabilities can be improved, and response to potential disaster situations can be addressed more effectively.

1.1. Aim of the Study

Many studies have been conducted in the literature to observe and detect the ground motion on the shaking table in the laboratory environment. In these studies, images are usually recorded utilizing a camera placed on the side of the table, and information about the direction and amount of movement is obtained by examining the reference lines drawn by hand (Zhang et al., 2006; Zhao et al., 2015). However, there are also studies in which image recordings were taken from the top of the experimental setup to get a rough idea of the movement (Lu et al., 2015). In such studies, situations such as the onset and development of cracks were examined through the records. In addition, there are studies that aim to detect landslide movements through fiber optic sensors (Hojat et al., 2019).

This thesis aims to conduct an in-depth study on detecting the movement of simulated landslides in a laboratory environment using image processing methods. For this purpose, the effectiveness of existing image processing techniques in detecting landslide motion will be evaluated, and potential improvements and enhancements will be proposed.

Image processing is the procedure of analyzing, rendering, and enhancing a digital image using computer programs. The first image-processing studies started in the 1960s. The foundations of image processing were laid with the development of analog image processing methods. In this period, image processing was mainly carried out with analog electronic systems due to the need for more computer power. With the increasing power of digital computers, digital image processing has gained importance. Digital processing methods were based on representing images with digital pixels. In the 1980s, significant advances were made, especially in medicine and radiology, and since the 2000s, it has been used in many different industries, such as media, automotive, security, and industrial automation.

The software was developed using Python programming language to detect and quantify the displacement of the sliding mass in the landslide simulator, where dynamic forces are applied considering different acceleration ranges and frequency content. In the experimental setup, a high-resolution camera is utilized for recordings during the experiments for later analysis with a Python code.The code has calibration sections for the correct operation of the system. Measurements made by tilt sensors and a laser measure were used to verify the measurements obtained from the software. The aim of the monitoring study employing image processing techniques is to establish a mechanism. This mechanism is designed to be activated through a shake table system, applying horizontal acceleration up to 0.5 g within frequencies ranging from 1 to 15 Hz. This simulation occurs on a laboratory-scale landslide simulator with a homogeneous, naturally sloping ground. The deformation verification using image processing applications allowed the evaluation of the implementation as a monitoring-early warning system in the field.

This study aims to provide a new perspective to the research in this field as an essential step in detecting landslide movements in a laboratory environment since early detection and mitigation of landslides are critical for future disaster management strategies.

1.2. Organisation of the Thesis

This thesis consists of seven chapters. In the introduction chapter, general information about the study is given, and the aim of the study is explained. The second chapter reviews previous studies in the literature that may inspire this study. The third chapter presents the theoretical background of the studies. Color models, pixel coordinate systems, and image processing stages are mentioned in this context. In the fourth chapter, the experimental setup and the equipment used are presented. The fifth chapter explains how the data from the experiments and video recordings were processed. Experimental results and related discussions are given in the sixth chapter. The last chapter offers conclusions from the entire process and suggestions for future studies.

2. LITERATURE SURVEY

One of the most dangerous natural hazards in the world, including Türkiye, is landslides. In Türkiye, they are recognized as a kind of disaster that is at least as significant as the risk of earthquakes or floods (Gökçe et al., 2008; Dağ and Bulut, 2012; Okalp and Akgün, 2016).

Several key factors contribute to reduced stability and mass failures at potential landslide sites: geomorphological parameters (slope angle, topography, etc.), precipitation regime (intensity, duration, frequency), groundwater levels (fluctuations, saturation), surface water variability (rivers, streams, infiltration), daily temperature differences (freeze-thaw cycles), and seismic activity from earthquakes and snowmelt. Many laboratory models have been developed in the literature to explain the process of underlying slope failures (Li and Cheng, 2014; Pajalic et al., 2021; Xie et al., 2021).

Sugiarto et al. (2023) developed a robot that employs a camera to receive information from objects to be tracked. This robot needed an image analysis containing data to recognize the objects around it. The information obtained through the images used as input data (output information) was characterized. The ball-wheeled robot could perceive its surroundings through visual input and make decisions aided by computer vision. It employed a combination of hue-saturation-value (HSV) color filtering and circle-hough transform (CHT) for object tracking. Using its front-facing camera and HSV color filtering, the robot could successfully detect a ball up to a distance of 1,000 cm. CHT was also used to improve the ball object recognition ability. A 700 cm distance was discovered to be sufficient to identify the ball. In addition, the ball could be specified up to 75% of the time when obscured.

Zhao et al. (2015) conducted experiments on a slope model created in a laboratory environment with varying frequencies and ranges of shaking. By amplifying movement and revealing specific vulnerabilities, the tests highlighted the limitations of the straight-form slope. The results help to understand the detailed collapsing behavior of the slope when an earthquake occurs. It provides crucial information for designing earthquake-resistant landslides and understanding their collapse mechanisms. The experimental setup used in the study is shown in Figure 5.

Figure 5. Slope model with accelerometers and displacement gauges (Zhao et al., 2015)

Yin et al. (2023) investigated the relationship between dust mass and image features such as grey levels and fractal dimensions in mining environments. Utilizing this knowledge, they developed a four-category hazard index and a deep-learning model for dust risk classification. This comprehensive approach provided a reliable and efficient tool for monitoring and analyzing mining dust pollution.

Lai et al. (2020) constructed a miniature replica and subjected it to simulated ground movements on a shake table to understand how cable-stayed bridges behave during earthquakes. They first analyzed the bridge's natural vibration patterns (modes) and then tested its response to two earthquake tremors: non-impact and impact near-fault. The bridge was built using natural materials - steel for the tower, girder and fasteners, and stainless steel for the crucial cables.

Lu et al. (2015) presented MUNOLD, a versatile landslide monitoring system comprising sensor networks, wireless communication, remote data storage, visualization tools, and advanced data analysis algorithms. Initial testing highlighted MUNOLD's potential for capturing real-time data on slope movement and expansion, while high-speed stereo imaging promises deeper insights into the critical stages of failure.

Born in the heart of fluid mechanics research, Particle Image Velocimetry (PIV) emerged in the 1990s as a revolutionary tool for dissecting the intricate dance of fluids. This technique, pioneered by Adrian (1991), sheds light on the hidden world of flow velocities by transforming the fluid into a canvas of motion. Tiny tracer particles, meticulously sprinkled throughout the fluid, become miniature dancers as their movements are meticulously captured by high-speed cameras. Analyzing the displacement of these "particle constellations" over time allows researchers to reconstruct the flow's velocity field with exquisite detail, unveiling the secrets of turbulent eddies, swirling vortices, and graceful laminar streams.

Zhang et al. (2006) look at how soil particle movement changes during a test at the soil-structure interface in this study. Images of the soil movement were taken using a high-speed camera, and quantitative data regarding the movement of soil particles were extracted using image processing techniques. To ascertain the velocity field of the soil particles and to examine the behavior of the soil-structure interface under various loading circumstances, the authors used the particle image velocimetry (PIV) technique. The outcomes of the image analysis offer a deeper comprehension of the interaction between soil and structure and can be applied to enhance the functionality and design of soil-structure systems.

The University of Tokyo's Geotechnical Engineering Laboratory's shaking table can generate two-directional horizontal movements. Researchers used a stacked accelerometer column as an inclinometer to measure tilt and strategically placed displacement gauges and accelerometers to capture the bridge's dynamic response. Vertical arrays of accelerometers were positioned below the crest, shoulder, and along the slope to monitor acceleration distribution within the slope model. A notable feature was the installation of colored square grids on the vertical glass wall, visually representing the model's dynamic deformation. Square grids in the photographs indicated shear failure or slippage at a certain depth beneath the surface, maintaining a moisture content of 1%. The team used particle image velocimetry (PIV) to investigate the slope's deformation under seismic loads. Researchers used the Particle Image Velocimetry (PIV) technique to study sand grain movement in simulated slope failures. By comparing two images taken at different times, they calculated the "cross-correlation" to measure how far individual sand grains had moved. This analysis, applied to shaking table models, revealed that displacement and velocity were highest above a specific "slip plane" where the simulated landslide occurred.

Fritz (2002) used laser speckle velocimetry (LSV) and large-scale digital particle image velocimetry (PIV) to measure the impulse waves created by landslides. He considered the difficulties in the measurement methods faced in a very erratic three-phase flow of water, air, and granular materials. The study analysed a particular part of the impulse wave generation region. A laser was used to control the lighting, and a camera was installed to view the system from the side. Subsequently, Fritz (2002) introduced the integrated analysis method for LSV on the landslide surface corona and PIV in water flow. Digital masking techniques also differentiated between phases, enabling phase-separated image processing.

White et al. (2021) applied the PIV method to images of ground materials such as natural sand or textured clay. For this purpose, image processing algorithms were written, and the software could measure ground movements with an accuracy of up to 1/15th of a pixel. A digital camera was used for image capture. To measure ground deformation, the natural texture of the ground was utilized instead of the traditionally used target markers. Thus, the deformation could be measured without interfering with the ground and with a higher sensitivity. The velocity fields obtained by the PIV method were used to calculate the soil parameters such as stress, strain, and shear angle. In addition, the results obtained with the PIV method were compared with other measurement methods and agreed well. The cost of the hardware and software required to measure soil deformation with the PIV method is lower than that of conventional methods. It is also emphasized that measuring a more comprehensive deformation range with the PIV method is possible.

Recently, studies have been carried out on a new type of material called transparent soil, which simulates natural soils. Its geotechnical characteristics are comparable to those of organic soil.

Bo et al. (2021) stated the following characteristics of transparent soil in their study:

- Since the transparent soil's refractive index matches or is nearly identical to the equivalent pore fluid, light can travel through it without refraction. Internal soil analysis is made possible with the help of this.
- Transparent soil provides robust technical support for model tests, simulating engineering issues within relatively complex geological engineering scenarios.
- The successful preparation of transparent soil relies on meticulous selection and combination of materials with precisely matched refractive indices. Key factors include the choice of aggregate (solid particles), pore solution composition, and controlled gas content within the mixture. Any deviation from optimal matching can compromise the desired transparency.
- Various elements, including objective and subjective, influence transparent soil transparency. Objective aspects include material qualities, preparation ratio, temperature, and humidity, as well as subjective ones like the knowledge and skill of the operators.
- It is essential to measure transparency accurately, and doing so quickly is an essential problem. Transparency may be measured quickly with the UV-2100 UV-visible spectrophotometer.
- Selection of appropriate aggregate type, pore solution composition, and mixture proportions is critical for optimizing the macroscopic properties of transparent soil, as variations in these elements can significantly impact its mechanical behavior, transparency level, and suitability for specific applications.
- The cost has been an issue due to the usage of various materials with varying costs and the variable nature of transparent soils.

Yuan et al. (2019) emphasized the characteristics of transparent soil mentioned in the study by Bo et al. (2021). The study delved deeper into the possibilities of transparent soil for studying internal soil behavior in geotechnical research. A transparent artificial soil recipe using amorphous silica powder and silica gel was developed in this context.

The study detailed an optical system utilizing a laser, a line-generating lens, and a digital camera to analyze how light interacted with the transparent soil. They also introduced digital image velocimetry (PIV) as a valuable tool for measuring soil displacement within the sample. Notably, the research highlights successful applications of transparent soil techniques in tackling various geotechnical challenges.

Hojat et al. (2019) observed pre-collapse cracks on recorded images and analyzed time-lapse ERT measurements to detect rainwater infiltration and development. Gallage et al. (2021) used a model box to study the effect of tilt angle on slope stability (Figure 6). The box was mounted on a frame that could be adjusted at five different angles. A soil consisting of a mixture of sand and clay was filled into the model slope box. An irrigation system used as a rain simulator was placed on the top of the model slope box. Two high-resolution cameras were placed on the front surface of the model slope box to monitor the slope deformation. The camera images were analyzed using image processing software. The image processing software identified the deformation areas by detecting color changes in the camera images. In addition, the image processing software calculated the deformation ratios by measuring the size and shape of the deformation areas.

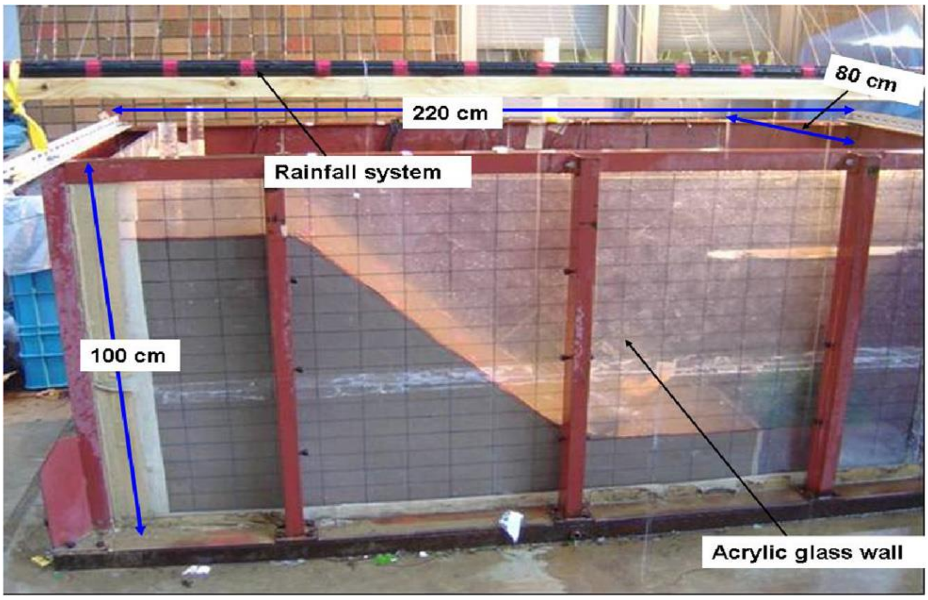

Figure 6. Model box with rainfall system (Gallage et al., 2021)

While object tracking aims to estimate or forecast an object’s position given its initial location across a video sequence, object detection identifies a target object within a single frame or image (de Vries et al., 2022; Delibaşoğlu, 2023; Tsai et al., 2023). These skills are critical for many computer vision applications, such as surveillance, autonomous cars, and robot navigation. There are two main situations in which object tracking usually happens. Throughout the video, single object tracking (SOT) keeps focus on a single target, while multiple object tracking (MOT) or multiple target tracking (MTT) tracks multiple things at once (Luo et al., 2021).

The color characteristics can reveal how an object appears. This characteristic has various applications; a color histogram is among the most popular. The color histogram displays the distribution of colors in an image. It displays all the different colors and the quantity of each color in the picture. The drawback of color histograms is that they only consider an object’s color, ignoring its texture and shape. As a result, two distinct objects may have the same histogram. The color histogram has been employed for tracking in a few works (Li and Zheng, 2004; Zhao, 2007; Fotouhi et al., 2011).

Montrasio et al. (2015) conducted numerous flume tests, including a laboratory-scale reproduction of a landslide event in 2009 in the Giampilieri area of northeastern Sicily. The sample soil was filled into a box fixed to the base of the flume tester. A rain simulator equipped with a pump and a spray system capable of producing different rainfall intensities was placed on the box. In the study, a camera was fixed on the side of the flume tester and recorded continuously during the experiment. After the experiment, the camera recordings were analyzed. When the landslide initiated, the onset time, displacement amount, and velocity of the sliding mass were determined from the camera recording. The experimental set-up and equipment layout is shown in Figure 7.

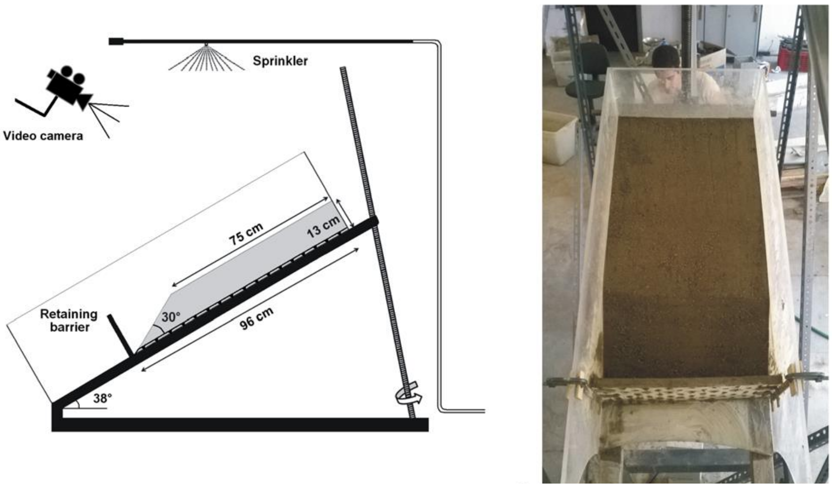

Figure 7. Rainfall triggered landslide container and equipment placement (Montrasio et al., 2015)

Fairman et al. (1997) explained how the CIE 1931 color matching functions were derived from mathematically modeling and how the human eye perceives colors. The study used the results of a series of experiments conducted by Wright and Guild in 1928-1929 to derive curves showing how the light of different wavelengths can be mixed into three primary colors (red, green, and blue). It also summarised the work done by the CIE to standardize these curves and define color space. The historical background and mathematical foundations of the CIE 1931 color matching functions, which formed an essential basis for color science and color imaging technologies, were explained in this study.

Buckley and Crean (1994) discussed the concept of device independence in color processing. Device-independent color specification employs colorimetric coordinates to articulate the visual stimuli required for achieving a desired color match. This specification ensures precise color representation irrespective of the specific printing device employed. The study introduced an architecture for device-independent color, facilitating the seamless addition of new devices to the system without impacting other computers or printers. This architecture allowed storing color images and documents in an independent device, enabling subsequent viewing or printing on any printer. However, the article recognized that device-independent color was a novel concept in the graphics arts field and was not universally embraced. Some argue it may not be suitable for producing offset-quality materials, citing fundamental disparities between computer monitor color and four-color ink-on-paper processes. The article also delved into the challenges associated with device-independent color in the print process. These challenges encompassed determining the gamut mapping intent, developing a black printer, and addressing process-related issues such as dot gain and trapping. It emphasized the importance of addressing these challenges to achieve accurate color representation in printed materials. In short, the study explored the concept of device-independent color and its application in the graphics arts field. It presented an architecture for device-independent color and discussed the challenges of achieving accurate color representation in printed materials.

Koenderink et al. (2021) explored the concept of object color from an ecological human biology perspective. They provided a minimalist formal account of object color and introduced various novel developments. The study defined object color as the surface scattering or reflection of environmental radiation, specifically daylight, on visual objects such as stones, apples, and rabbits. The use of a tripartition in colorimetry, which involved comparing the ratio of volumes in a linear space, which is a significant factor in object color formalism, allowing for quantitative comparisons was discussed. They also compared the CIE-xy diagram with an orthographic projection and discussed the latter's benefits in providing an intuitive representation of color. The concept of hue and the parameterization of different choices for each hue was explored, and the Ostwald atlas, which consisted of pages representing different hues in a triangular, barycentric scheme, was mentioned. They explained that canonical spectra can be good approximations to actual spectra in some instances. The article concluded by addressing the limitations of color as a label for objects, highlighting the variability of color perception and the potential for color deception in a hypothetical world with fake objects and sources. The evolutionary purpose of color was questioned, and it was suggested that it may be useless for hunter-gatherers. The study presented a minimalist formal account of object color and discussed various color perception and representation aspects. It provided insights into the ecological human biology perspective on object color and its implications regarding vision and evolution.

When the studies in the literature were analyzed, the camera was used as an auxiliary element, and image recordings were used as auxiliary data in almost all studies that use artificial landslides or shaking tables. Unlike the literature, in this thesis, camera and video recordings are integrated into the center of the study as the primary measurement tool. The main purpose of the study is to use these recordings as a measurement mechanism with the help of image processing. Other measurements will be made to verify the image processing data.

3. THEORY

3.1. RGB Color Model

The RGB color model is foundational in digital imaging and light-based media. Developed in the late 19th century based on the Young-Helmholtz theory of trichromatic vision and subsequently supported by Maxwell's color triangle, it utilizes the additive combination of red, green, and blue primary light to represent a wide range of color hues. This additive approach, contrasting with subtractive models like CMYK used in color printing, enables the generation of a diverse color gamut from a limited set of fundamental colors. Consequently, the RGB model has become a dominant standard in digital screens, projectors, and other light-emitting technologies. While not alone in the realm of color models, RGB occupies a significant position alongside CMYK and RYB (red, yellow, blue). While CMYK reigns supreme in subtractive color mixing for print media, RYB holds historical significance in traditional artistic practices. In conclusion, the RGB color model is a cornerstone of contemporary visual representation through its efficient and versatile approach in generating a vast spectrum of colors from a minimal set of primary light components (Zelazko, 2023). Figures 8 and 9 show these color models in their simplest form.

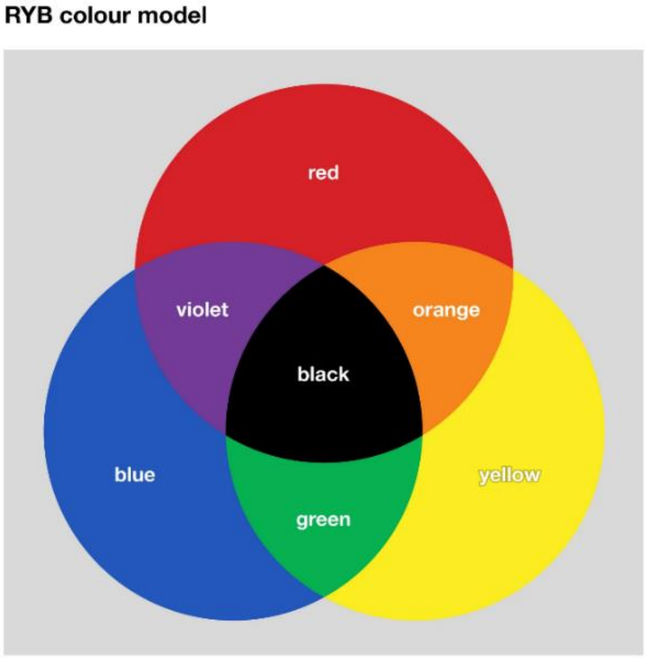

Figure 8. RYB Color Model

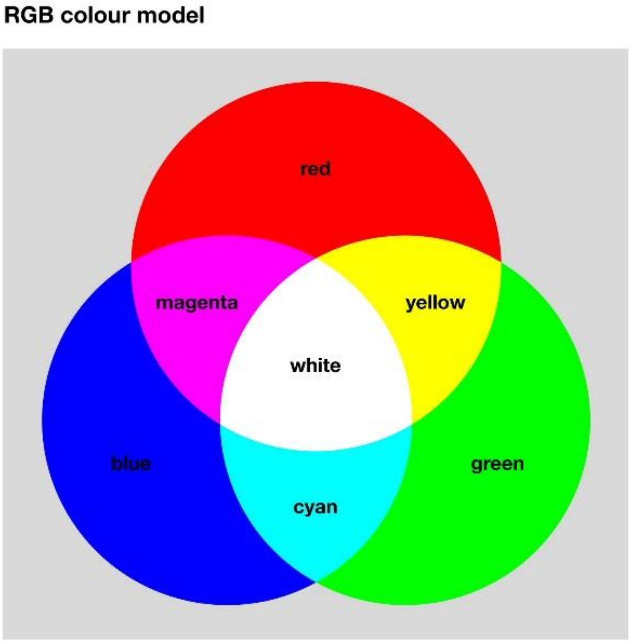

Figure 9. RGB Color Model

While finding some application in traditional photography, the RGB color model primarily serves as the dominant method for capturing, representing, and displaying visual information in electronic devices like computers and televisions. Interestingly, its theoretical foundation, grounded in human color perception, predates the advent of the electronic age (Fairman et al., 1997).

The RGB color model relies on the device's characteristics, as the color components (like phosphors or dyes) and their reactions to red, green, and blue levels can differ between manufacturers or even change within the same device over time. Various devices may interpret or render a specific RGB value in distinct ways. Consequently, without color management, a given RGB value does not represent the same color consistently across different devices (Crean & Buckley, 1994).

Digital cameras, image scanners, and color TVs are examples of standard RGB input devices. The RGB color model finds diverse applications in output devices encompassing various display technologies, including cathode ray tubes (CRTs), liquid crystal displays

(LCDs), plasma screens, organic light-emitting diodes (OLEDs), quantum dot displays, computer and smartphone screens, video projectors, multi-color LED displays, and grand-scale displays like Jumbotrons. Contrarily, color printers are subtractive color devices that usually use the CMYK color model rather than RGB devices.

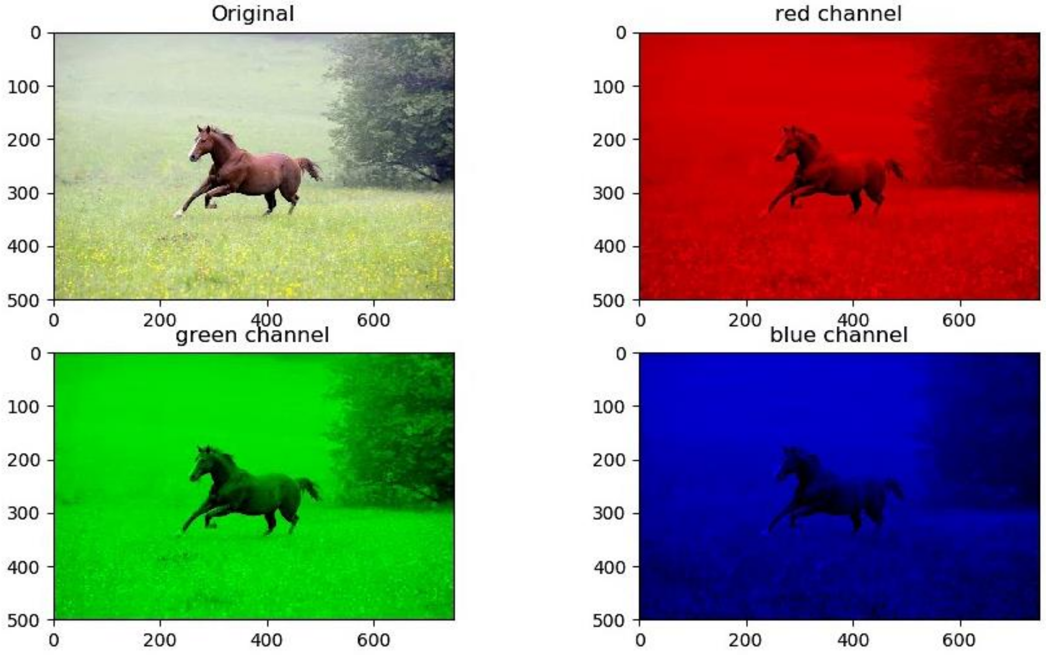

Figure 10. Full-color image along with its R, G, and B components

Beyond its established role in digital color representation, RGB extends its reach into the realm of electronics as a high-quality component video signal. This format transmits the vital red, green, and blue color information as independent signals through dedicated cables or pins, akin to separate streams converging to paint a vibrant visual display. Modified versions of established monochrome video standards like RS-170 and RS-343 often provide the foundation for these robust RGB formats. Since the highest quality signal can be transmitted using a conventional SCART connector, this video transmission is extensively utilized throughout Europe.

RGB is not a standard video signal format outside of Europe; most non-European regions use S-Video. Nonetheless, RGB is used by practically all computer monitors worldwide.

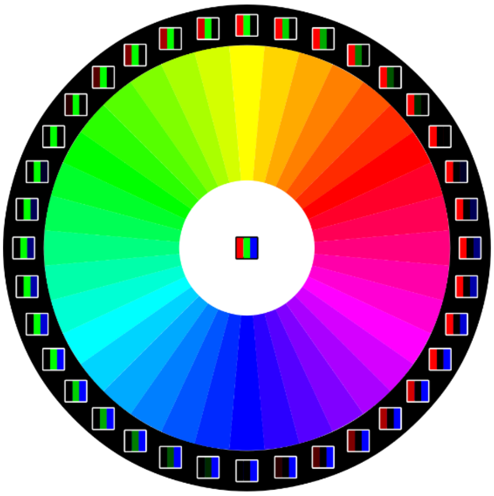

Figure 11. RGB pixel representation of a color wheel

Before the 1990s, color televisions and video cameras used prisms and filters to divide incoming light into the three primary RGB colors. Each color was then fed into a different video camera tube, also known as a pick-up tube. Not to be confused with the tubes used in cathode ray tube displays, these tubes are a type of cathode ray tube.

The commercialization of CCD technology in the 1980s marked a major shift in video capture. Replacing the limitations of video camera tubes, CCDs enabled the development of smaller, more integrated cameras with improved image quality and performance. Subsequently, smaller home video cameras were made possible using more highly integrated electronics, simplifying or eliminating the need for intermediate optics and creating complete camcorders. The miniaturization trend culminates in the ubiquitous webcams and smartphone cameras in our daily lives, representing the pinnacle of image capture technology in its most compact form.

In the RGB color model, the amount of each red, green, and blue component that makes up a color is used to describe it. The RGB triplet (r, g, b) representing the color can have values ranging from zero to a predetermined maximum for each component. The outcome is black if every component is zero and the brightest representable white if every component is maximum.

There are various methods to quantify these ranges:

- In color representation, percentages express the proportions of each primary color (red, green, and blue) that make up a specific hue, ranging from 0% to 100%.
- Inside computers, however, color components typically take the form of unsigned integers, spanning from 0 to 255. They align with the capacity of an 8-bit byte, the fundamental digital storage unit. These values are commonly displayed in either decimal or hexadecimal format.
- Advanced digital imaging devices often offer a wider range of integer values for each color component, reaching up to 1023 in 10-bit systems and an impressive 65535 in 16-bit systems. This system's expanded color depth is achieved by extending the standard 24-bit format (which utilizes three 8-bit values) to larger units like 32-bit, 48-bit, or even 64-bit. Notably, this enhanced color representation is not significantly constrained by the word size of the computer itself. For example, the brightest saturated red is written in the different RGB notations in Table 1.

R: 213

G: 111

B: 56

Figure 12. A standard RGB color selector used in graphics programs. The range of each slider is 0 to 255.

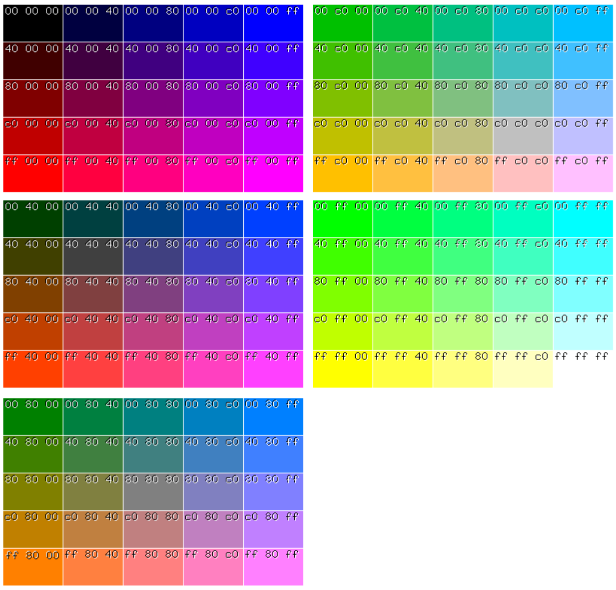

00 00 00	00 00 40	00 00 80	00 00 c0	00 00 ff	00 c0 00	00 c0 40	00 c0 80	00 c0 c0	00 c0 ff
40 00 00	40 00 40	40 00 80	40 00 c0	40 00 ff	40 c0 00	40 c0 40	40 c0 80	40 c0 c0	40 c0 ff
80 00 00	80 00 40	80 00 80	80 00 c0	80 00 ff	80 c0 00	80 c0 40	80 c0 80	80 c0 c0	80 c0 ff
c0 00 00	c0 00 40	c0 00 80	c0 00 c0	c0 00 ff	c0 c0 00	c0 c0 40	c0 c0 80	c0 c0 c0	c0 c0 ff
ff 00 00	ff 00 40	ff 00 80	ff 00 c0	ff 00 ff	ff c0 00	ff c0 40	ff c0 80	ff c0 c0	ff c0 ff
00 40 00	00 40 40	00 40 80	00 40 c0	00 40 ff	00 ff 00	00 ff 40	00 ff 80	00 ff c0	00 ff ff
40 40 00	40 40 40	40 40 80	40 40 c0	40 40 ff	40 ff 00	40 ff 40	40 ff 80	40 ff c0	40 ff ff
80 40 00	80 40 40	80 40 80	80 40 c0	80 40 ff	80 ff 00	80 ff 40	80 ff 80	80 ff c0	80 ff ff
c0 40 00	c0 40 40	c0 40 80	c0 40 c0	c0 40 ff	c0 ff 00	c0 ff 40	c0 ff 80	c0 ff c0	c0 ff ff
ff 40 00	ff 40 40	ff 40 80	ff 40 c0	ff 40 ff	ff ff 00	ff ff 40	ff ff 80	ff ff c0	ff ff ff
00 80 00	00 80 40	00 80 80	00 80 c0	00 80 ff					
40 80 00	40 80 40	40 80 80	40 80 c0	40 80 ff					
80 80 00	80 80 40	80 80 80	80 80 c0	80 80 ff					
c0 80 00	c0 80 40	c0 80 80	c0 80 c0	c0 80 ff					
ff 80 00	ff 80 40	ff 80 80	ff 80 c0	ff 80 ff					

Figure 13. Hexadecimal 8-bit RGB representations of the primary 125 colors

Table 1. RGB values for the brightest saturated red

Notation	**RGB triplet**
Arithmetic	(1.0, 0.0, 0.0)
Percentage	(100%, 0%, 0%)
Digital 8-bit per channel	(255, 0, 0) #FF0000 (hexadecimal)
Digital 12-bit per channel	(4095, 0, 0) #FFF000000
Digital 16-bit per channel	(65535, 0, 0) #FFFF00000000
Digital 24-bit per channel	(16777215, 0, 0) #FFFFFF000000000000
Digital 32-bit per channel	(4294967295, 0, 0) #FFFFFFFF0000000000000000

3.2. Pixel Coordinate System

The pixel coordinate system is a concept used in digital imaging and computer graphics. A pixel (picture element) is the smallest element of a digital image. Pixels are the colored dots that make up an image. A pixel coordinate system is a structure in which these pixels are arranged in a specific order.

Typically, a two-dimensional plane is used to define the pixel coordinate system. This plane represents a rectangular image. There are two coordinate axes, usually called the x and y axis. The x-axis usually represents coordinates in the horizontal direction of the image, while the y-axis usually represents coordinates in the vertical direction (Zhang et al., 2023).

The pixel coordinate system increments its units starting from the upper left corner. For example, the point (0,0) usually corresponds to the upper left corner of the image, while the point (1,0) corresponds to just to the right of this point. Similarly, point (0,1) is positioned one pixel down from the upper left corner, and point (1,1) is positioned to the right and one pixel down.

This coordinate system is frequently used in image processing, computer graphics, game programming, and similar fields. Each pixel is usually associated with a color value, so the pixel coordinate system is a fundamental tool in creating and manipulating digital images. The pixel coordinate system layout in an image is shown in Figure 14.

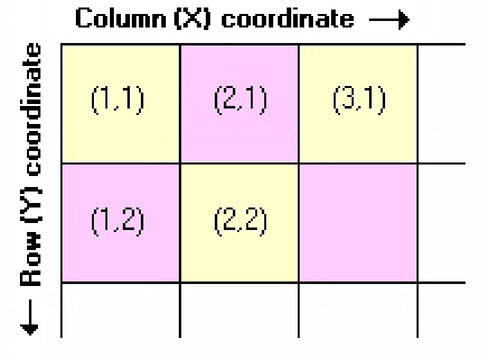

Figure 14. Image pixel coordinate system

Origin: The origin (0, 0) is the reference point at the image's top-left corner or screen. The x-coordinate increases horizontally to the right, and the y-coordinate increases vertically downward. This convention is commonly used in computer graphics.

Positive Axes: The positive x-axis extends to the right from the origin, and the positive y-axis extends downward. Negative values on these axes extend in opposite directions.

Resolution: The resolution of an image is defined by the number of pixels in the horizontal (width) and vertical (height) directions. For example, an image with a resolution of 800 x 600 has 800 pixels along the x-axis and 600 pixels along the y-axis.

Quadrants: The coordinate plane is divided into four quadrants. Quadrant I is in the positive x and y directions, Quadrant II is in the negative x but positive y directions, Quadrant III is in the negative x and y directions, and Quadrant IV is in the positive x but negative y directions.

Units: In the pixel coordinate system, the unit of measurement is the pixel. Each pixel represents a discrete point on the display, and the resolution of the display determines the number of pixels per unit length.

Integer Values: Pixel coordinates are typically expressed as integers. For example, a pixel at coordinates (3, 4) would be the fourth pixel to the right and the fifth pixel down from the top-left corner.

Sinusoidal signals, or analog signals, are used by traditional televisions to display images. Digital technology underlies monitors for computer systems. Pixels comprise the image displayed on the monitor: rows of tiny dots. Every pixel has a corresponding color. The eye detects a continuous image rather than individual dots when the dots are small enough and closely spaced apart. An image is represented by its dimensions (height and width) based on the number of pixels. For instance, if an image's width and height are 600 x 500, its total pixel count is 300000. Personal computer monitors (PCs) typically have the following recording resolutions: 800(horizontal) by 600(vertical), 1024 by 768, 1280 by 1024, 1600 by 1900, 1920 by 1080, 2560 by 1440, 2560 by 1600, and 3840 by 2160. Generally speaking, the resolution and possible quality of the image increase with the amount paid. The quantity of colors related to every pixel is another essential consideration. In monochrome displays, such as black and white or amber and black, every pixel is associated with just two colors. Other frequent associations are 256 colors per pixel, 32,768 colors, 65,536 colors, and 16,777,216 colors per pixel. The pallet is the collection of available colors. The amount of storage needed to store and/or display the image has historically been the primary constraint on the size of the pallet (number of colors).

In summary, the pixel coordinate system is a simple and intuitive way to represent the positions of points in a 2D space, commonly used in computer graphics, image processing, and related fields. The origin, positive axes, resolution, quadrants, and units are critical concepts in understanding and working with the pixel coordinate system.

3.3. Digital Image Processing

Digital image processing refers to a category of techniques that employ computer algorithms to manipulate digital images. It is a crucial preprocessing stage in various applications, including face recognition, object detection, and image compression. A digital computer uses algorithms to process images (Chakravorty, 2018; Gonzalez, 2018). Since images are defined in at least two dimensions, digital image processing can also be considered a multidimensional system. The evolution of computers, advancements in mathematics (especially the growth and refinement of discrete mathematics theory), and the increasing demand across diverse fields like environment, agriculture, military, industry, and medical science have collectively influenced the creation and progression of digital image processing. Figure 15 shows some basic operations that can be performed with image processing.

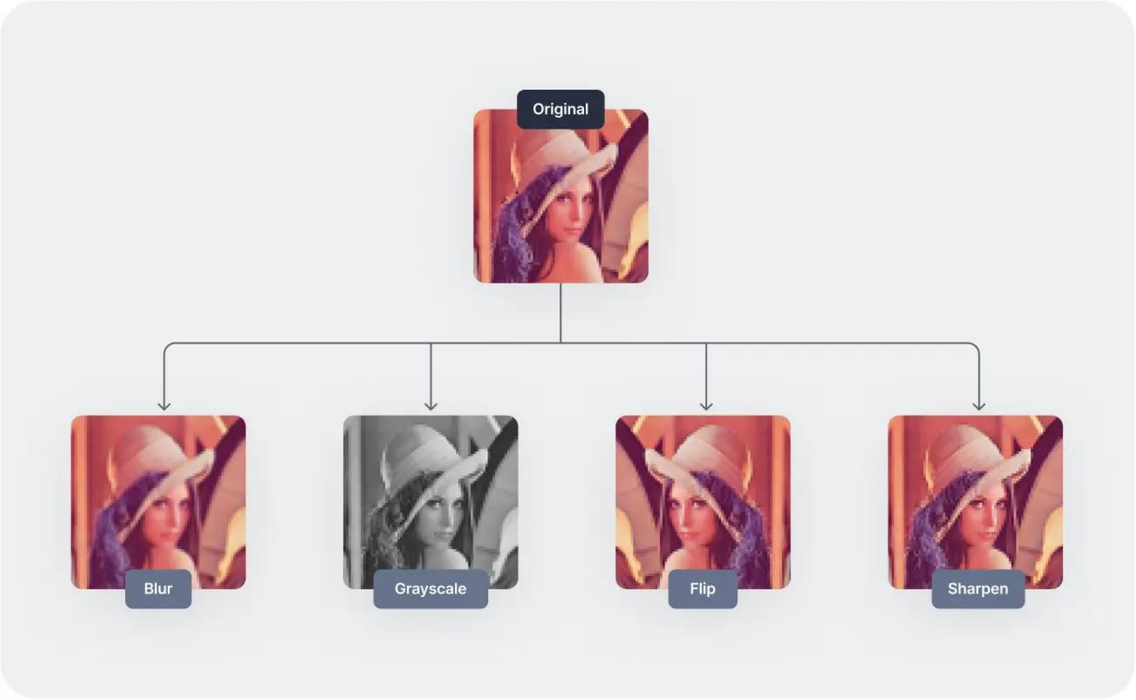

Figure 15. Examples of basic image processing operations

3.3.1. Types of Images

Digital images, in the computer's view, are not mere visual representations but rather discretized functions within a multi-dimensional space. These functions, typically expressed as “I(x, y) or I(x, y, z),” map each pixel (a discrete point within the image lattice) to a specific intensity or color value. In the prevalent 8-bit format, this value ranges from 0 (absolute darkness) to 255 (peak brightness), quantifying the light captured at that particular point.

For monochromatic (grayscale) or binary images, the function operates within a two-dimensional domain (I(x, y)). Each pixel intensity within this domain represents the grayscale level or binary state (on/off) based on its position within the image matrix. Conversely, RGB images necessitate a three-dimensional function (I(x, y, z)), as each pixel is defined by the contributions of three independent channels: red, green, and blue. Understanding these functions and their underlying mathematical framework is crucial for manipulating, analyzing, and interpreting digital imagery in various computational contexts. Computers handle various “types” of images according to their function representations (Kundu, 2023).

3.3.1.1. Binary Image

Binary images have two possible pixel intensity values: 0 for black and 1 for white. These pictures are usually used to draw attention to a specific area of a colored picture. As demonstrated below, image segmentation is one common application for it.

3.3.1.2. Grayscale Image

Images in grayscale or with an 8-bit color depth exhibit a limited palette of 256 distinct hues. Pixel intensity directly translates to color within this spectrum: 0 signifies absolute black, while 255 represents pure white. All intermediate values (254 shades) depict varying degrees of gray. Figure 16 illustrates the transition from an RGB image to its grayscale counterpart, highlighting the preservation of the overall histogram shape despite the reduction in color information.

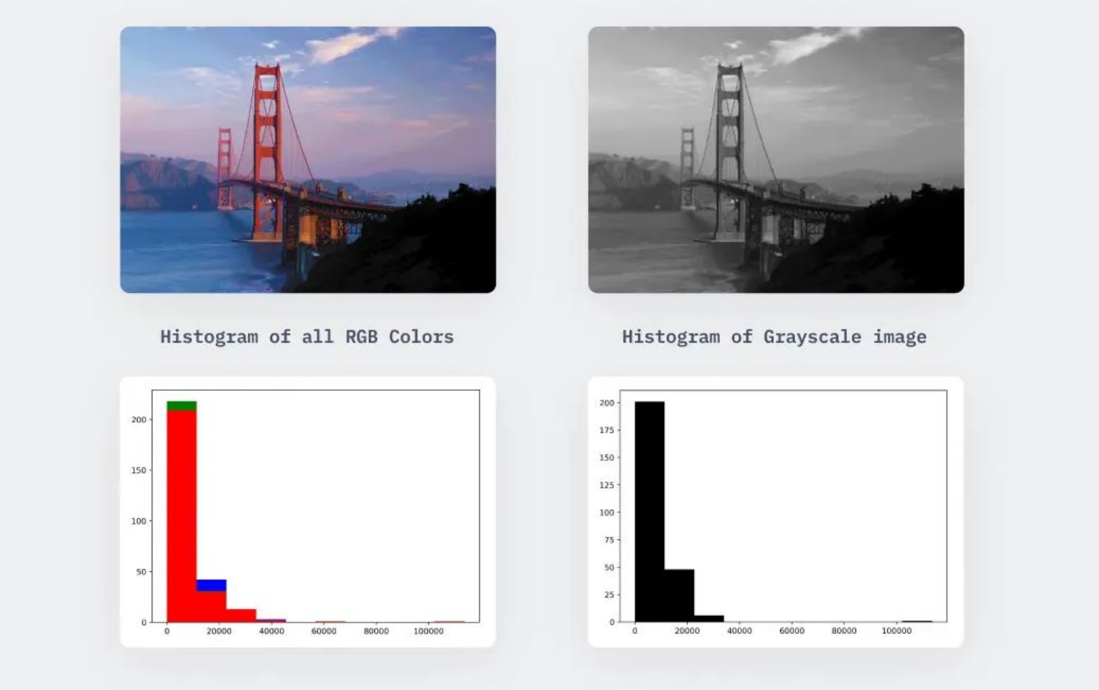

Figure 16. Examples of RGB images converted to its grayscale version

3.3.1.3. RGB Color Image

As explained in the previous sections, RGB or colored images, which are represented by 16-bit matrices by computers, are what we are accustomed to seeing in the modern world. That is, every pixel can have 65,536 possible color combinations.

3.3.1.4. RGBA Image

RGBA images are RGB images that have been colored, plus an additional channel called "alpha" that shows how opacity is applied to the RGB image. Opacity is basically a "see-through" quality, with a value ranging from 0% to 100%.

In physics, opacity describes how much light can pass through an object. For example, wood is opaque, frosted glass is translucent, and cellophane paper is transparent (100 percent opacity). In RGBA images, the alpha channel attempts to replicate this characteristic, demonstrated in Figure 17.

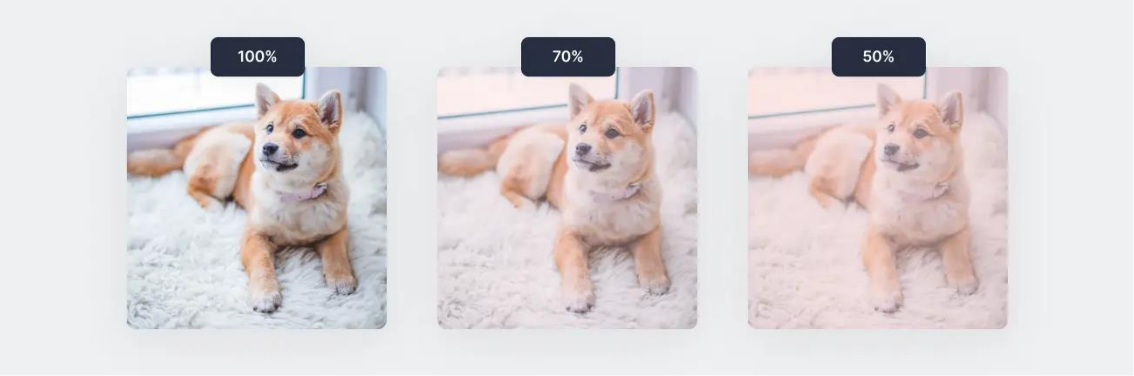

Figure 17. Examples of customizing the "alpha" parameter in RGBA images

3.3.2. Phases of Image Processing

The following are the basic steps in any standard workflow for digital image processing.

3.3.2.1. Image Acquisition

An analog-to-digital converter is used to digitalize the image after a camera takes it, and if the camera output is not already digital, it is used so that it can be processed further in a computer.

3.3.2.2. Image Enhancement

This step involves modifying the obtained image to make it suitable for the particular purpose for which it will be used. These methods mainly focus on an image's subtle or significant details, such as brightness and contrast adjustments. The process of enhancing an image is very subjective.

3.3.2.3. Image Restoration

This step is inherently objective due to the ability to model image degradation using well-defined mathematical or probabilistic frameworks. It enables the application of quantifiable methods and algorithms to address common issues like noise reduction and blur removal, ultimately enhancing the image's perceptual quality and information content.

3.3.2.4. Color Image Processing

Focusing on multi-channel, 16-bit color images (RGB or RGBA), this phase addresses specific demands for color modeling and correction, leveraging tailored algorithms and processes.

3.3.2.5. Wavelets and Multi-Resolution Processing

The fundamental units used to represent images at different resolutions are called wavelets. Images are successively subdivided into smaller regions for pyramidal representation and data compression.

3.3.2.6. Image Compression

Images cannot be stored at their original size and must be compressed to be transferred to other devices or because of limitations on computational storage. This process is crucial regarding how images are displayed online; for instance, a thumbnail image is a significantly reduced original version on Google. The image's original resolution is only displayed when it is clicked. This procedure conserves the servers’ bandwidth.

3.3.2.7. Morphological Processing

It is necessary to extract image components for tasks that require further processing or downstream that help represent and describe shapes. The means to achieve this are provided by morphological processing, a set of mathematical operations. For instance, the edges of objects in an image can be sharpened or blurred using the erosion and dilation operations, respectively.

3.3.2.8. Image Segmentation

In this step, an image is divided into several essential components to simplify and/or transform its representation into something more understandable and straightforward to examine. Image segmentation improves the performance of automated systems by allowing computers to focus on the more significant portions of the image and ignore the rest.

3.3.2.8. Representation and Description

Post-segmentation, image representation involves deciding how to depict segmented regions as either boundaries or complete areas. This choice paves the way for description, extracting attributes that quantify relevant information or differentiate object classes.

3.3.2.9. Object Detection and Recognition

The automated system must give an object a label once the objects have been separated from an image and the representation and description stages have been finished. This label should indicate to human users what kind of object has been detected, such as “person” or “vehicle.”

3.3.2.10. Knowledge Base

For an object of interest located in the image, the bounding box coordinates and object label can provide all the information needed to identify it. Everything that can assist in resolving the issue for the particular task at hand can be added to the knowledge base.

4. EXPERIMENTAL STUDY

4.1. Development of Laboratory Model

Numerous studies have been carried out to examine various sliding mechanisms and the impact of triggering factors to understand the mechanism of slope failure (Moriwaki et al., 2004; Arslan et al., 2015; Atmajati et al., 2017; Zhou et al., 2016; Lo and Weng, 2017; Morse and dig., 2017; Hojat et al., 2019; Ma et al., 2019). Each researcher has used multiple models and triggering mechanisms. This study aims to trigger a mass movement on an artificial soil utilizing a laboratory-scale slope container on a shaking table capable of applying different accelerations in the horizontal direction. The simulations for this purpose were carried out on a shake table installed in the Earthquake Simulation Laboratory of the Civil Engineering Department of Hacettepe University, which was established with the support of TÜBITAK within the scope of the ARDEB-1001 research project.

Various factors are considered to determine the size of the landslide container that should be placed on the shaking table, including the maximum velocity, motion characteristics, maximum deformation, damping motions, and plane strain. By putting plexiglass sheets at the bottom of the system, the boundary effect is designed to be reduced along the vibration direction. The size effect and the shaking of the table capacity are the two main variables that affect the shaking dimensions of the shaking table when vibration is applied (Wood, 2004). Typically, the depth of the sliding plane to the length (D/L) of the model scale is used to compute rotational slips in the lab (Abramson et al., 2002). Additionally, the width-to-height ratio (W/H) of the model must be selected appropriately to maximize floor height and minimize the impact of lateral friction based on height. With all of this information, a shaking table measuring 2 m in length, 1.1 m in width, and 0.16 m thickness, with a capacity of 1.8 tons, a maximum frequency of 15 Hz, and a system that can apply horizontal acceleration up to 0.5g was designed for laboratory simulation studies (Figures 18, 19 and 20).

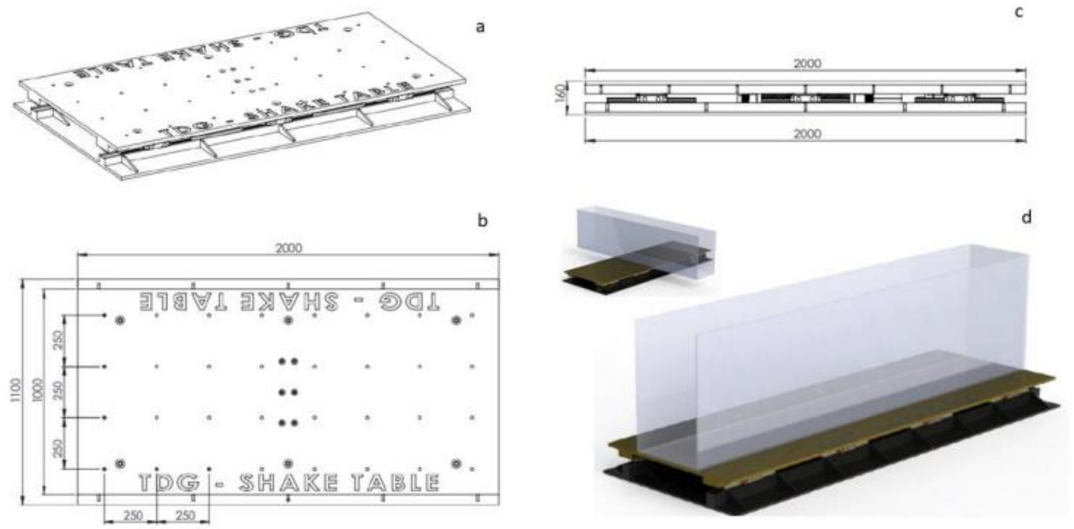

Figure 18. a) View of the shaking table, b) plan view of the shaking table, c) cross-sectional area of shaking table, d) plexiglass landslide container

The plexiglass landslide container, which is 2 m in length, 0.55 m in width, and 0.80 m in height, can be rotated and fixed if required, allowing horizontal acceleration testing in various directions. The technical drawing and details of the test setup are given in Figure 21. Figure 18d shows an alternative scenario for a landslide with acceleration in opposing directions.

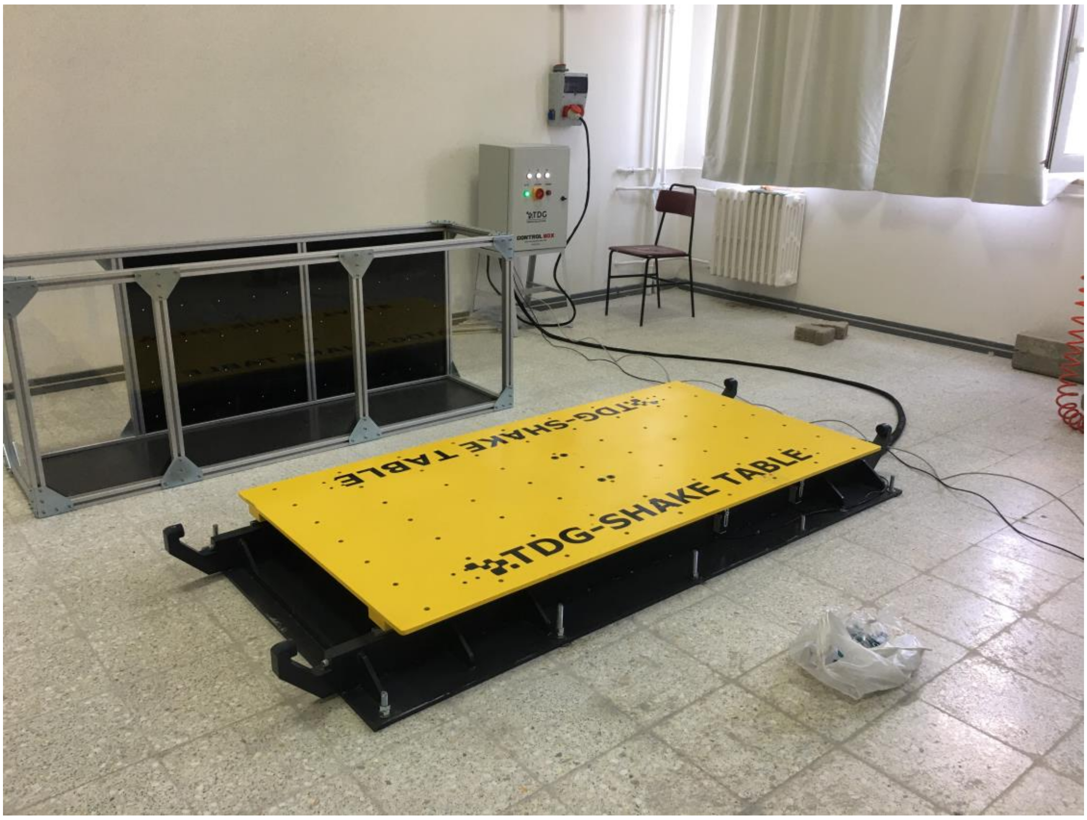

Figure 19. View of shaking table before installation of landslide container

Figure 20. View of landslide container and shaking table after installation

A data acquisition system with 16 channels and software is used to operate the shaking table (Figure 22). In addition to the predefined motion options within the program, users can also import acceleration records of an earthquake of their choice. In addition, the user can create and import record files in which instantaneous acceleration values are entirely defined.

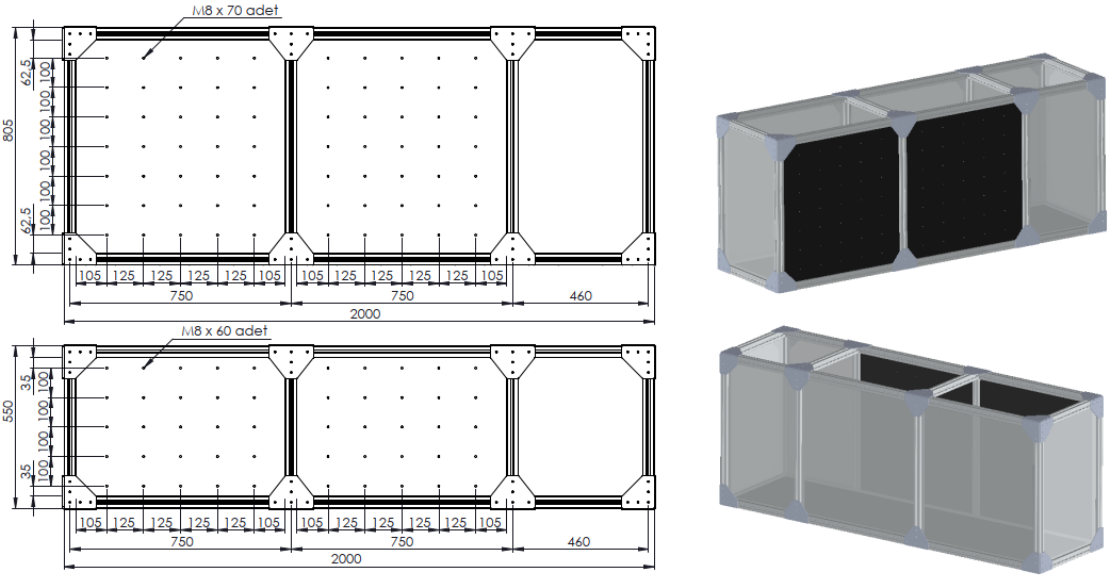

Figure 21. Technical detail of landslide container

It is feasible to identify the features of soil behavior that might influence how the sliding mass moves within the landslide container based on acceleration or displacement of the sliding mass by conducting repeated tests with the dynamic landslide simulator. The sloping landslide soil model was subjected to dynamic forces while considering dynamic earthquake parameters at varying frequencies and with horizontal acceleration.

A data logger connects the shaking table and the computer **(**Figure 22**)**. LVDT or triaxial accelerometers can also be connected to this device for data acquisition. Through the software designed for the system, the data from the data logger can be read, and the movements of the shaking table can be adjusted.

Figure 22. Data logger that is connected to shake table

Image recordings of the experiments were taken with a DJI Osmo Action camera (Figure 23). The measurements were made with a laser pointer and slope tilt sensors placed in the sand, and the relationship between them was examined to check and verify the amount of deformation measured by image processing.

Figure 23. DJI Osmo Action High-Resolution Camera

DJI Osmo Action with a 12 MP sensor resolution and a wide field of view of 145 degrees was used in image acquisition. With a single-frame view, it could see the entire landslide formation in a single frame and record 60 frames per second at 4K and 2.7K resolution and 240 frames per second at 1080p resolution. The recordings were taken at 60 frames in 1080p resolution, which was thought to provide sufficient sensitivity in image processing studies. Since the camera moved with the shake table, it was exposed to vibrations. In addition, since it was predicted that this situation would have adverse effects during the image processing phase, the recordings were taken using the anti-vibration feature of the camera. As a result of the examinations made of the images, it was determined that the vibrations were largely eliminated. In addition, the camera could be fixed to the experimental setup with the help of sigma profiles and provided close-ups. Continuous video recording could be taken for about one hour in Full HD quality with a full charge. Also, a 5-metre charging cable was provided for longer recordings. Raw images recorded on the Samsung 256GB Evo Plus Micro Sd card were stored on external discs in (DNG) and JPEG format at regular intervals.

The angle difference between the tracked object and the camera should be at a minimum level to achieve maximum accuracy in the amount of deformation to be detected while processing the received image records. If the angle difference increases, detecting the presence of motion is still possible, but the margin of error in digitizing the motion in terms of deformation increases. Considering this issue in camera placement, a camera stand was formed with the help of sigma profiles. This stand was mounted on the shaking table, and the final camera position was determined, as shown in Figures 24, 25 and 26.

Figure 24. Camera stand mounted on the landslide container

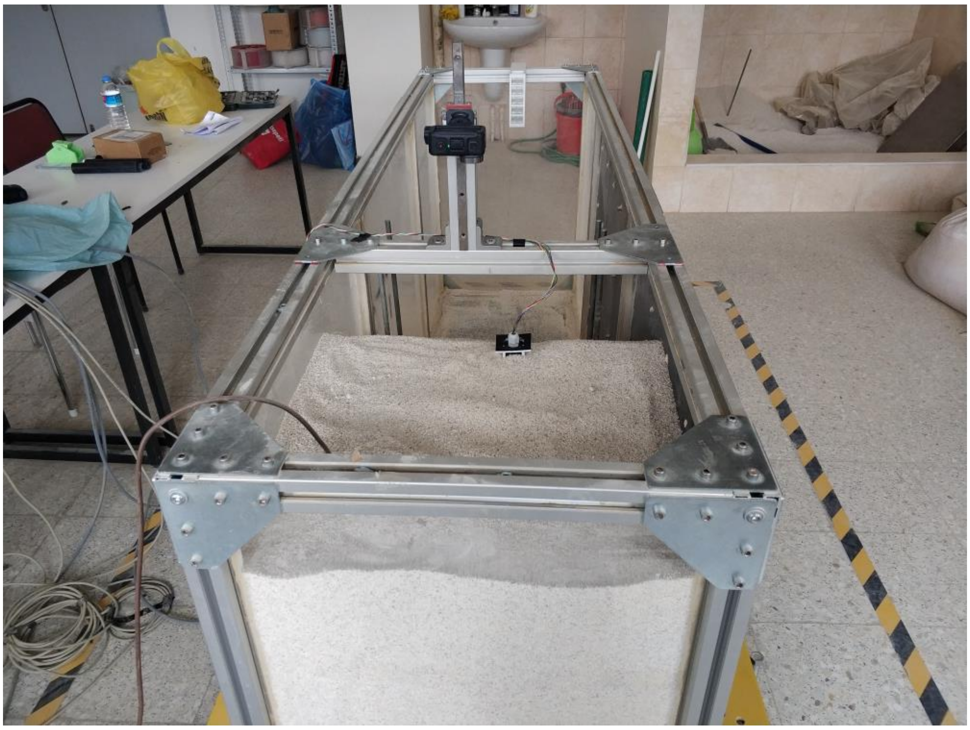

Figure 25. The view of camera placement in the landslide container

Figure 26. The plan view of the camera placement

In the current installation, surface deformation readings can be determined with image recordings. Verification with different measurement methods is necessary to check the accuracy of the data obtained or to examine the relationship between them. For this reason, two tilt sensors were placed in the experimental setup. One of these sensors was designed to be close to the base, and one close to the surface. For the placement of the sensors, tilting pipe and joint designs were made to be printed on a 3D printer (Figures 27 and 28).

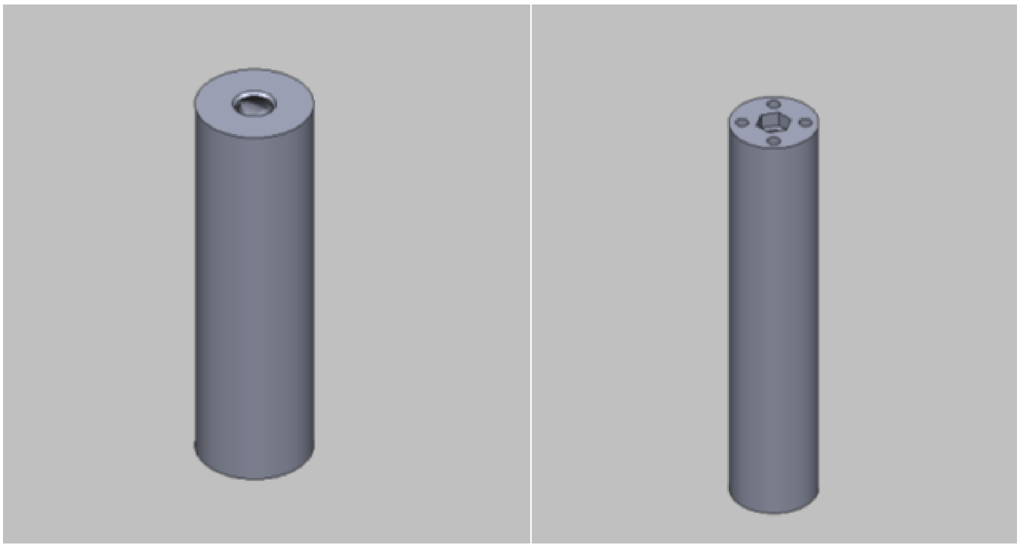

Figure 27. Pipe designs for tilt sensors

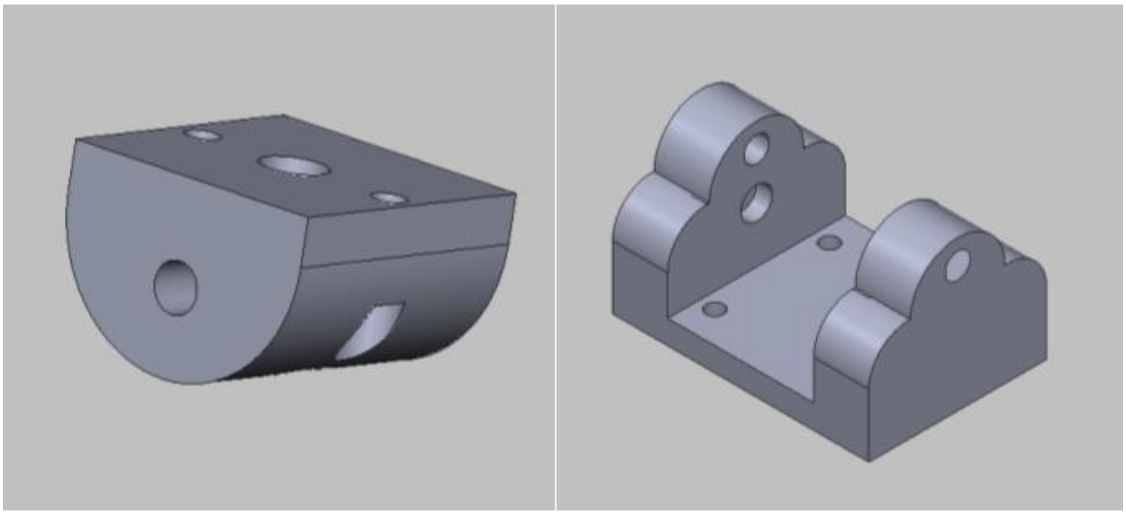

Figure 28. Articulated joint design for pipe connection

After the sensors were placed in the pipes, they were placed on a Plexiglas floor and fixed to the base of the shaking table. With the two tilt sensors placed, the development of the mass movement in the lower layers could also be monitored. By this way, it should be possible to draw the projection of the movement. The sensors' cable connections and the tilting pipe placement in the landslide container are shown in Figures 29 and 30.

Figure 29. Tilt sensor cable connections and mounting of the tilting pipe on the shaking table

Figure 30. Positioning and top view of the tilting pipe

The data received from the tilt sensors could be transferred to the computer environment with the help of special software called Witmotion. With the aid of the software, the slope angle values measured by the sensor could be monitored instantaneously. It also allows multiple sensors to work together at the same time. Thus, the slope angle values at the beginning and end of the experiment are recorded, and it is controlled whether there is an unusual development during the experiment. Figure 31 shows the software interface.

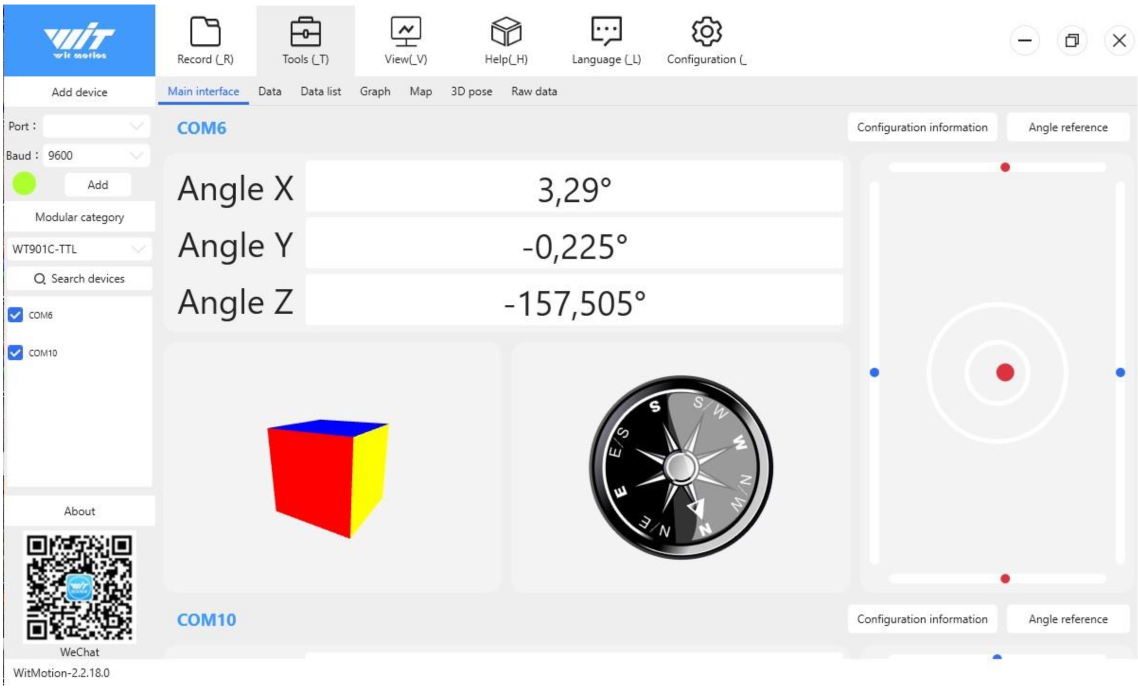

Port :

Baud : 9600

Modular category: WT901C-TTL

☑ COM6

☑ COM10

COM6

Angle X 3,29°

Angle Y -0,225°

Angle Z -157,505°

COM10

WitMotion-2.2.18.0

Figure 31. Instant data acquisition from the tilt sensor with Witmotion software

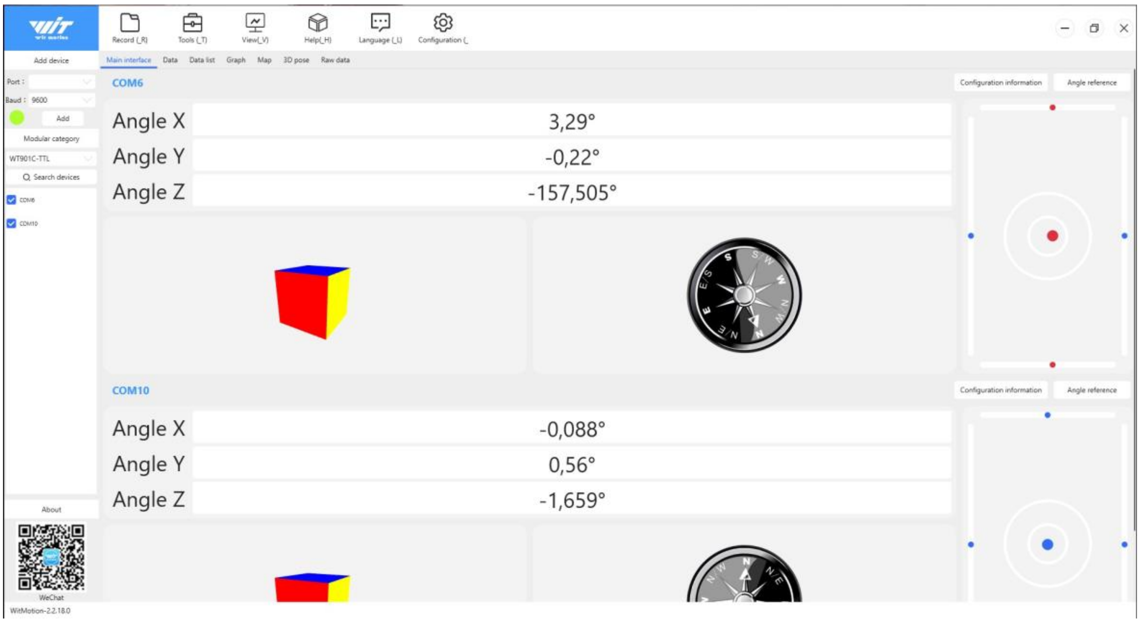

Port :

Baud : 9600

Modular category: WT901C-TTL

☑ COM6

☑ COM10

COM6

Angle X 3,29°

Angle Y -0,22°

Angle Z -157,505°

COM10

Angle X -0,088°

Angle Y 0,56°

Angle Z -1,659°

WitMotion-2.2.18.0

Figure 32. Data acquisition system over multiple sensors

As mentioned in the previous sections, the RGB value of pixels will be used in image processing studies. At this point, an object to be accepted as a reference on the image was needed. In this context, a 5 x 5 cm tracking plate was designed to be placed on the top of the tilt sensors on the landslide container and printed with a 3D printer. This plate was painted black to form a contrast with the sand. Thus, the experiments created an apparent reference zone on the white-colored sand. The plate and its placement are shown in Figures 33 and 34. A side view of the experimental setup is given in Figure 35.

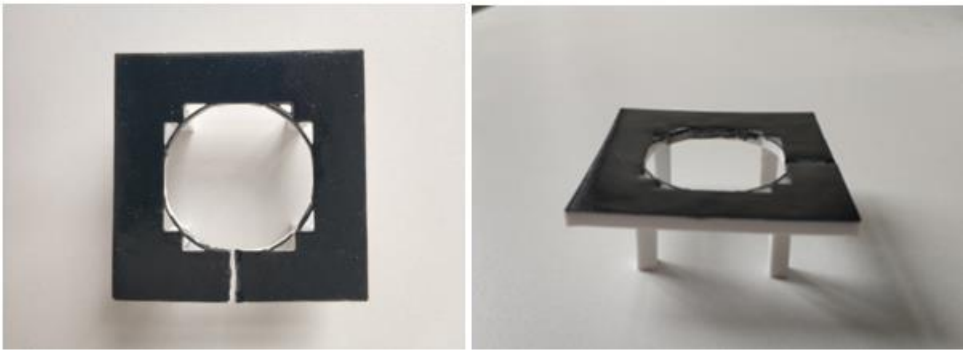

Figure 33. 3-D printed tracking plate for the tests

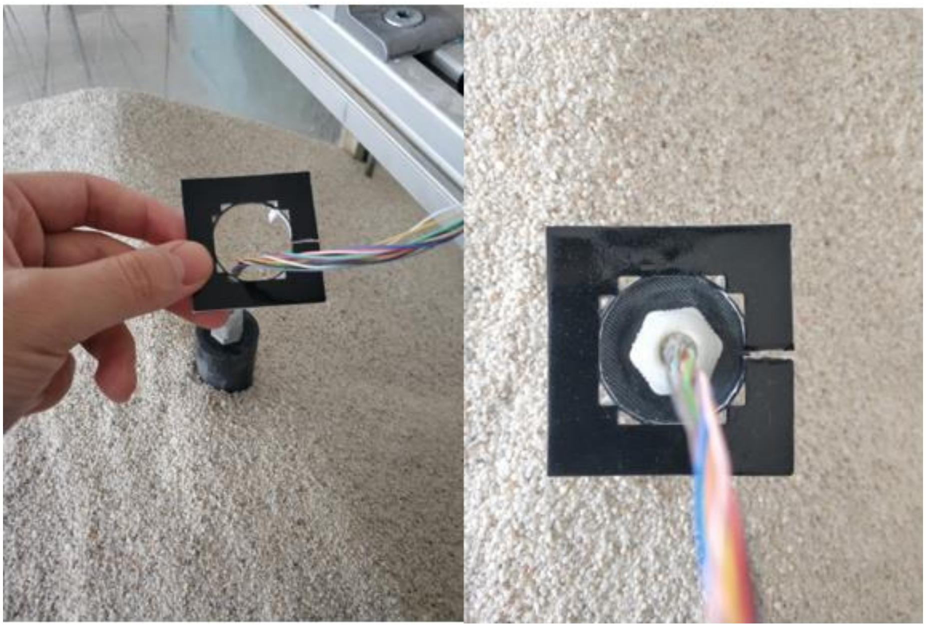

Figure 34. Tracking plate placement in the experimental setup

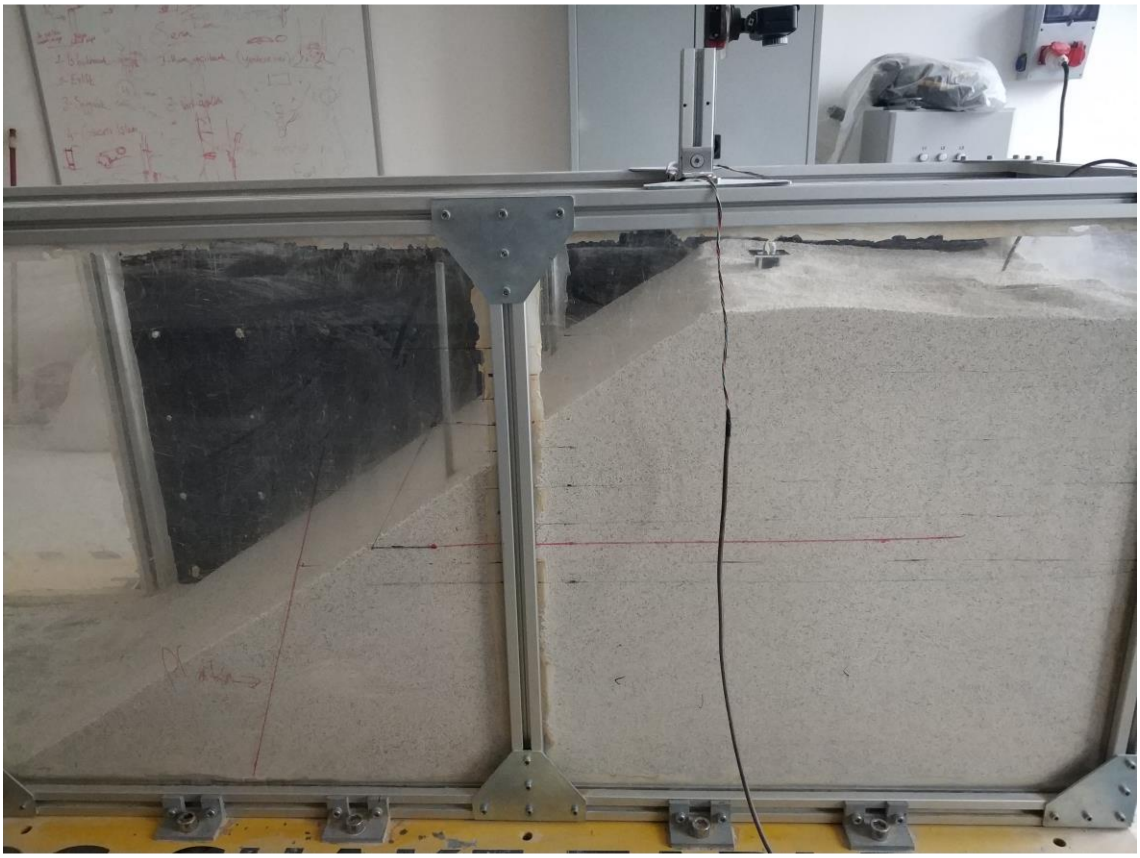

Figure 35. A side view of the experimental setup

The distance per pixel is the main parameter for image processing studies. This length must first be known to calculate the amount of movement of the object tracked through the image. One calibration photograph was taken with all parts and the camera in their standard positions on the experimental setup to determine this length. This photograph selected the number of pixels on one edge of the tracking plate with a known edge length (5 cm). This length was measured as 161 pixels. Therefore, each pixel corresponded to a distance of 0.322 mm. The calibration photograph is shown in Figure 36.

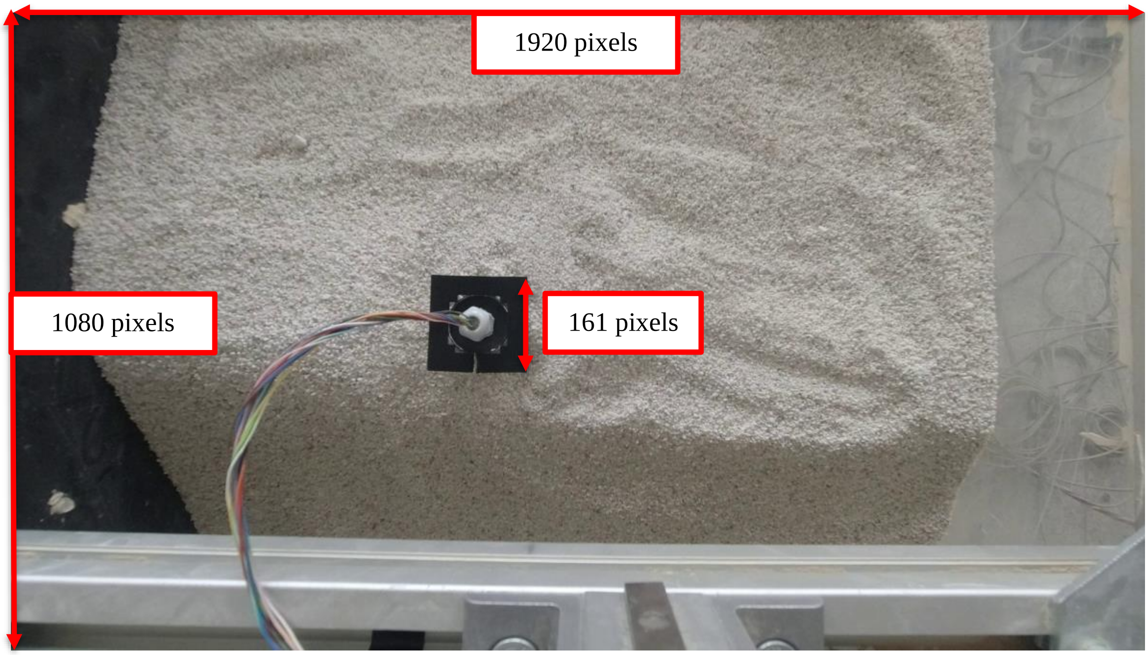

Figure 36. A view of the calibration photograph

In addition to the tilt sensor and image processing, direct measurements were taken using a laser measurement system (Figure 37). Bosch GLM 50 C Professional was used for these measurements. The maximum measurement distance of the device is 50 meters, and it can measure in millimeters. In addition to distance measurement, the device can also be used for angle measurements and alignment applications. It is also dust resistant and, therefore, suitable for use in a laboratory environment. It is a known fact that the precision of this method is relatively low compared to others, but it is a good option as a third control point to follow the development of the movement and to evaluate it together with other data. Therefore, it was decided to add it to the experimental setup.

Figure 37. The laser measurement system used in the experimental setup

A measurement positioning apparatus has been designed and printed with a 3D printer to ensure a standard in laser measurements (Figure 38). The fact that the designed apparatus is composed of sub-slots allows measurements to be taken from different elevations (Figure 39). This slot, which is produced in such a way that it can be placed on any edge of the shaking table by passing it into the gaps of the sigma profiles, does not require any screwing process for assembly. This apparatus allows measurements to be taken at the same reference point after each experiment. Figure 40 shows a view of laser measurement in an experiment.

Figure 38. The view of the measurement positioning apparatus

Figure 39. The placement of the laser measurement system in the positioning apparatus

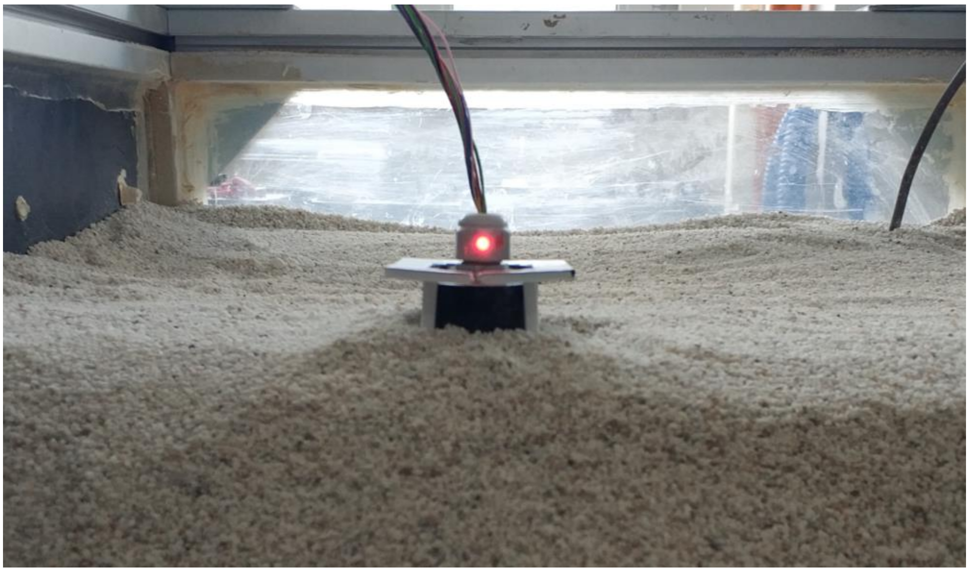

Figure 40. The view of the laser measurement system in the experiment

4.2. Geotechnical Properties of Soil Sample Used in the Research

A sieve analysis test was performed to determine the index soil properties (i.e., sieve analysis) of sand-size sediments used in the landslide container. As a result of the grain size distribution curve, it was determined that the sand material has a grain size in the range of 0.8 to 2 mm and is poorly graded coarse sand (SP) according to the USCS system. Table 2 and Figures 41 and 42 show these test results with the soil classification results, respectively.

Table 2. Sieve analysis test results

Sieve No.	Mass Retained (g)	Cumulative Mass Retained (g)	Percentage Retained (g)	Cumulative Percentage Retained (g)	Cumulative Percentage Passing (g)	Sieve Opening (mm)
No 4	0.5	0.5	0.05	0.05	99.95	4.75
No 10	3.1	3.6	0.31	0.36	99.64	2
No 20	772	775.6	77.12	77.48	22.52	0.85
No 40	214.4	990	21.42	98.90	1.10	0.425
No 60	2.6	992.6	0.26	99.16	0.84	0.25
No 100	2.5	995.1	0.25	99.41	0.59	0.15
No 140	1.7	996.8	0.17	99.58	0.42	0.106
No 200	1.3	998.1	0.13	99.71	0.29	0.075
Pan	2.9	1001	0.29	100.00	0.00	

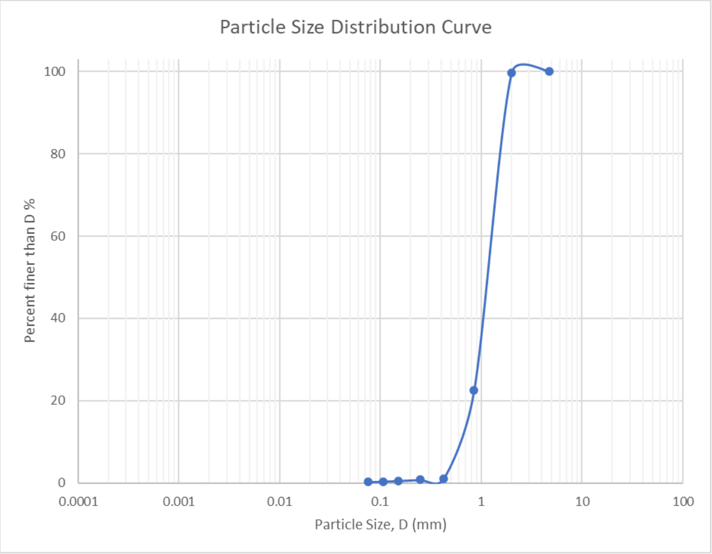

Figure 41. Grain size distribution curve of the sand material

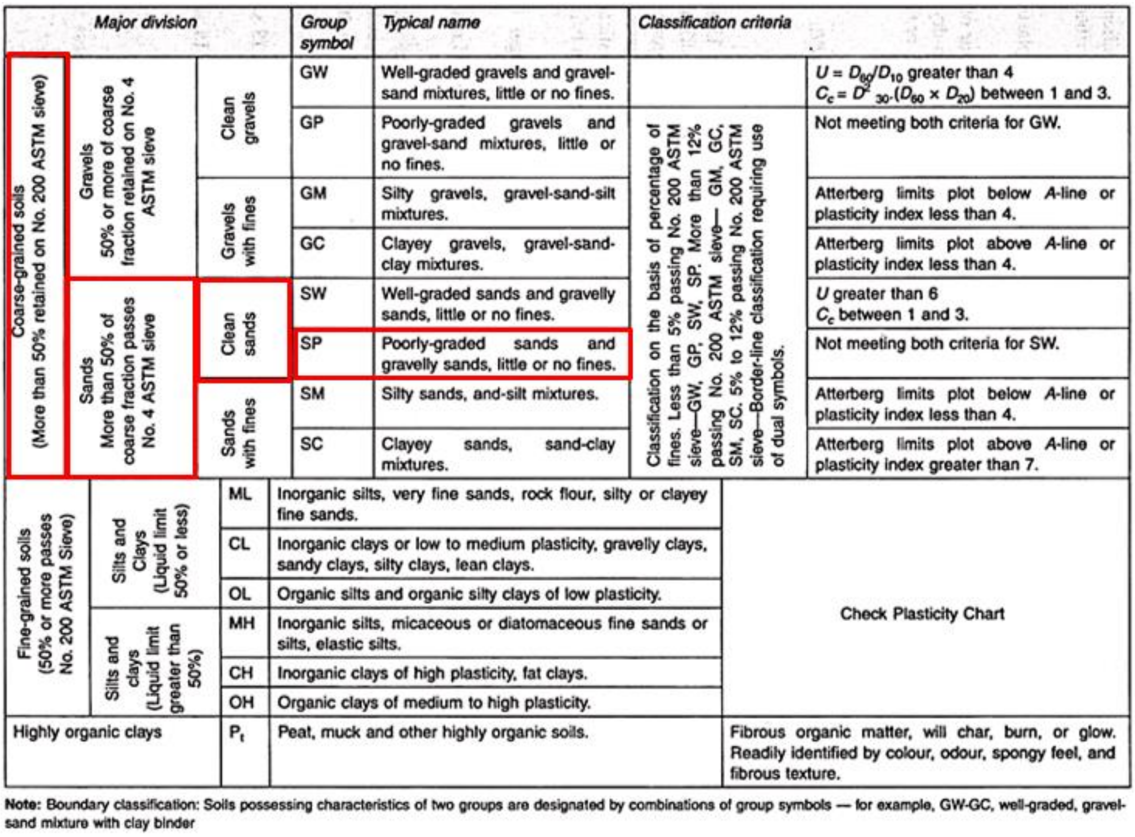

Major division			Group symbol	Typical name	Classification criteria	
Coarse-grained soils (More than 50% retained on No. 200 ASTM sieve)	Gravels 50% or more of coarse fraction retained on No. 4 ASTM sieve	Clean gravels	GW	Well-graded gravels and gravel-sand mixtures, little or no fines.		$U = D_{60}/D_{10}$ greater than 4 $C_c = D^{2}{}_{30}\cdot(D_{60} \times D_{20})$ between 1 and 3.
			GP	Poorly-graded gravels and gravel-sand mixtures, little or no fines.	Classification on the basis of percentage of fines. Less than 5% passing No. 200 ASTM sieve—GW, GP, SW, SP. More than 12% passing No. 200 ASTM sieve— GM, GC, SM, SC. 5% to 12% passing No. 200 ASTM sieve—Border-line classification requiring use of dual symbols.	Not meeting both criteria for GW.
		Gravels with fines	GM	Silty gravels, gravel-sand-silt mixtures.		Atterberg limits plot below *A*-line or plasticity index less than 4.
			GC	Clayey gravels, gravel-sand-clay mixtures.		Atterberg limits plot above *A*-line or plasticity index less than 4.
	Sands More than 50% of coarse fraction passes No. 4 ASTM sieve	Clean sands	SW	Well-graded sands and gravelly sands, little or no fines.		*U* greater than 6 C_c between 1 and 3.
			SP	Poorly-graded sands and gravelly sands, little or no fines.		Not meeting both criteria for SW.
		Sands with fines	SM	Silty sands, and-silt mixtures.		Atterberg limits plot below *A*-line or plasticity index less than 4.
			SC	Clayey sands, sand-clay mixtures.		Atterberg limits plot above *A*-line or plasticity index greater than 7.
Fine-grained soils (50% or more passes No. 200 ASTM Sieve)	Silts and Clays (Liquid limit 50% or less)		ML	Inorganic silts, very fine sands, rock flour, silty or clayey fine sands.	Check Plasticity Chart	
			CL	Inorganic clays or low to medium plasticity, gravelly clays, sandy clays, silty clays, lean clays.		
			OL	Organic silts and organic silty clays of low plasticity.		
	Silts and clays (Liquid limit greater than 50%)		MH	Inorganic silts, micaceous or diatomaceous fine sands or silts, elastic silts.		
			CH	Inorganic clays of high plasticity, fat clays.		
			OH	Organic clays of medium to high plasticity.		
Highly organic clays			P_t	Peat, muck and other highly organic soils.	Fibrous organic matter, will char, burn, or glow. Readily identified by colour, odour, spongy feel, and fibrous texture.	

Note: Boundary classification: Soils possessing characteristics of two groups are designated by combinations of group symbols — for example, GW-GC, well-graded, gravel-sand mixture with clay binder

Figure 42. Soil classification results according to the Unified Soil Classification System (USCS)

A specific gravity test was performed to determine the material density. According to the results of the test, it was determined that the specific gravity value of the slope material was 2.69. Table 3 shows the specific gravity test results. Table 4 shows that the internal friction angle of poorly graded sands are between 30-39 degrees (Bek et al., 2021; Geotechdata.info, Angle of Friction, 2013). A direct shear test was performed to determine the shear strength characteristics of the material. The internal friction angle was determined as 39^{o}. Table 5 and Figure 43 display the shear strength parameters of the sand determined by direct shear testing.

Table 3. Specific gravity test results

Test temperature	20°C		
Trial No.	1	2	3
Mass of dry pycnometer (M_p)	39,5	40,1	39,8
Volume of pycnometer (V_p)	100	100	100
Mass of pycnometer filled with only water at test temperature ($M_{pw,t}$)	143,7	143,6	142,2
Mass of pycnometer, water, and soil solids at the test temperature ($M_{\rho ws,t}$)	181,3	179,5	174,1
Mass of Pan and Soild soil (g)	151,2	157	153,3
Mass of Pan (Mp) (g)	93,5	99,6	100,7
Mass of the oven dried soil solids (M_s)	57,7	57,4	52,6
Specific gravity of solids at the test temperature	2,87	2,67	2,54

Table 4. Values of the internal friction angle in coherent and cohesionless soils (Bek et al., 2021; Geotechdata, Angle of friction)

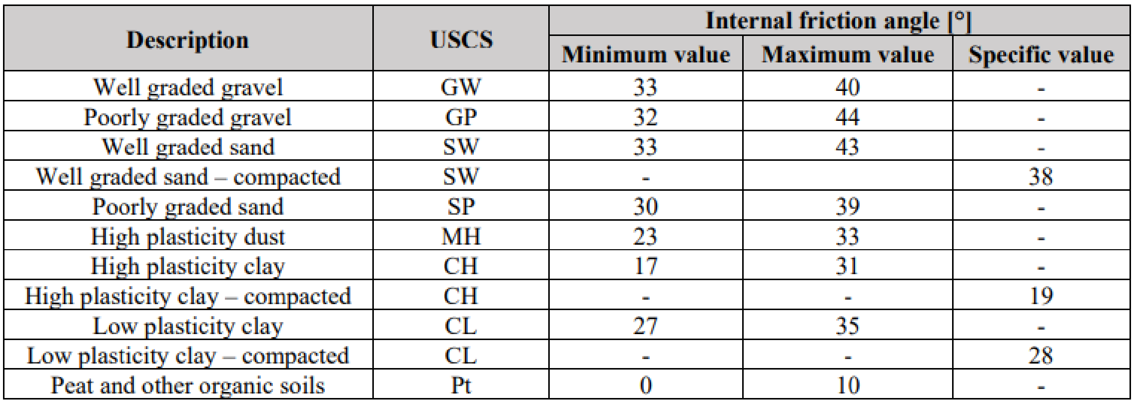

Description	**USCS**	**Internal friction angle [°]**		
		Minimum value	**Maximum value**	**Specific value**
Well graded gravel	GW	33	40	-
Poorly graded gravel	GP	32	44	-
Well graded sand	SW	33	43	-
Well graded sand – compacted	SW	-		38
Poorly graded sand	SP	30	39	-
High plasticity dust	MH	23	33	-
High plasticity clay	CH	17	31	-
High plasticity clay – compacted	CH	-	-	19
Low plasticity clay	CL	27	35	-
Low plasticity clay – compacted	CL	-	-	28
Peat and other organic soils	Pt	0	10	-

Table 5. Direct shear testing results

	Normal Stress (kPa)	Shear Strength (kPa)
1	15,7	12,9
2	31,5	32
3	62,9	52,8

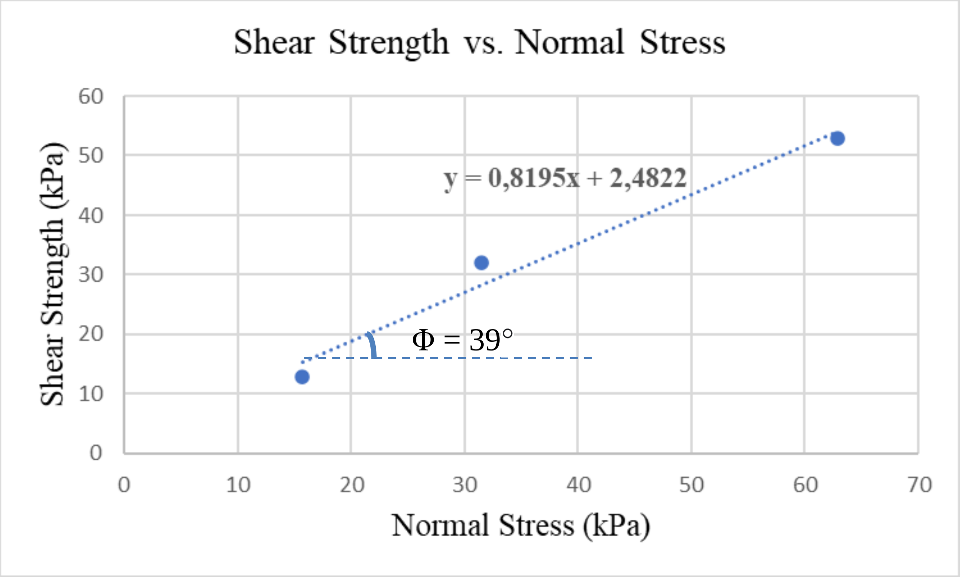

Figure 43. The plot of the shear strength vs. normal stress

5. DATA ANALYSIS

5.1. Extracting Frames from a Video and Modifying Images

The video recordings taken during the experiment were stored on an external disk. A code was needed to process the videos. This section will explain how to extract frames from a video using Python and OpenCV and then modify them by converting them to grayscale and adding annotations. We will walk through the code step by step and explain each component in detail. The full version of the code will be given in Appendix A.

5.1.1. Key Concepts

Before proceeding to the coding stage, the key concepts are explained below:

1. **Video Processing:** Video processing involves manipulating and analyzing video frames. In this case, individual frames from a video file are extracted.
2. **Frame Extraction:** Frame extraction refers to capturing individual frames from a video. Each frame represents a single image in the video sequence.
3. **Grayscale Conversion:** Grayscale conversion is converting an image from color to grayscale. Grayscale images only contain shades of gray, ranging from black to white, and are often used for image processing tasks.
4. **Image Annotation:** Image annotation involves adding visual elements, such as circles, rectangles, or text, to an image. Annotations can highlight specific regions or provide additional information about the image.

5.1.2. Code Structure

The code consists of three main sections: frame extraction, grayscale conversion, and image annotation. Each section is divided into parts, and its aim is explained below.

5.1.2.1. Frame Extraction

The first section of the code focuses on extracting frames from a video file. The procedures are organized as follows:

1. **Import the necessary libraries:** The code begins by importing the required libraries, including os, PIL, cv2, numpy, and matplotlib.pyplot.
2. **Define the video path and output directory:** The code specifies the path to the input video file and the directory where the extracted frames will be saved.
3. **Open the video file:** The code uses the cv2.VideoCapture function to open the video file for reading.
4. **Iterate over the frames:** The code enters a loop that reads each frame from the video using the cap.read() function. If the frame is successfully read, it is saved as an image using the cv2.imwrite() function. The frame count is incremented, and the progress is displayed.
5. **Release the video capture object:** Once all the frames have been extracted, the code releases the video capture object using the cap.release() function.

5.1.2.2. Grayscale Conversion

The first section of the code focuses on extracting frames from a video file. The procedures are organized as follows:

1. **Define the img2gray function:** This function takes an image as input and converts it to grayscale using the formula gray = np.dot(img[..., :3], [0.299, 0.587, 0.114]). The function returns the grayscale image.
2. **Define the process_images function:** This function uses input and output folders as parameters. It iterates over the files in the input folder, reads each image using plt.imread(), converts it to grayscale using the img2gray function, and saves the grayscale image using plt.imsave().
3. **Specify the input and output folders:** The code prompts the user to enter the input and output folder names.
4. **Start the image processing:** The code calls the process_images function with the specified input and output folders to convert the images to grayscale.

5.1.2.2. Image Annotation

The third section of the code focuses on adding annotations to the grayscale images. The steps are explained below:

1. **Define the annotation functions:** The code defines three functions: draw_circle, draw_rectangle, and draw_text. These functions use the Image Draw module from the PIL library to draw circles, rectangles, and text on the images.
2. **Define the process_image function:** This function uses input and output paths as parameters. It opens the image using Image.open(), processes the image by calculating the mean coordinates of specific pixel values, and adds annotations using the annotation functions. The modified image is then saved using image.save().
3. **Specify the input and output directories:** The code specifies the input and output directories for the image processing.
4. **Process the images:** The code iterates over the files in the input directory, selects specific images to process based on their index, and calls the process_image function to add annotations to the images.

The video recording is ready to be processed by defining the file location of a video for the code to run and then the folder names where the processed images will be saved. Due to the large number of frames extracted from the video, the processed images take up much space in file size. The code has been modified to process the desired number of frames at the beginning and end of the video without interruption and to process one frame out of every 10 frames in the intermediate sections. Thus, the size of the result files is reduced, and an advantage is provided in terms of storage.

As a result of running the code within the scope of image processing, the frames separated from the video are first saved in their original form (colored images). Then, they are converted into grayscale, and the location of the tracking plate is determined. This process is done by filtering the RGB values, which are accepted as boundary values, on the image. The code detects the pixels that meet the conditions, and the center point is determined, and a frame is drawn around it. By this way, the position of the tracking plate is recorded over the images at the beginning and end of the video, and the distance traveled is determined in pixels. The distance corresponding to a pixel is also combined with the recorded data using the calibration process described in Section 4.1, and the image processing results for a representative data set are generated, as shown in Table 6. The final analyses of the image processing data for comparison with tilt sensor and laser measurements have been developed and presented in Appendix A. A sample frame extracted from an experiment video is shown in Figure 44, and the processing on this frame is shown in Figures 45 and 46.

Figure 44. A frame extracted from the video recording

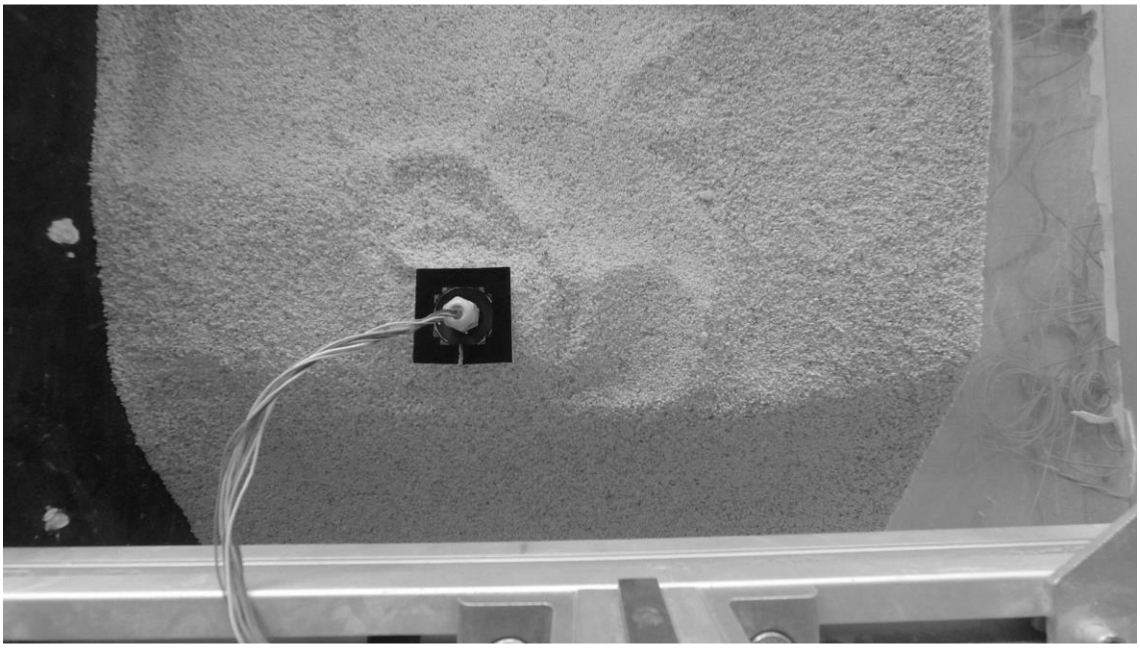

Figure 45. A grayscale version of the frame

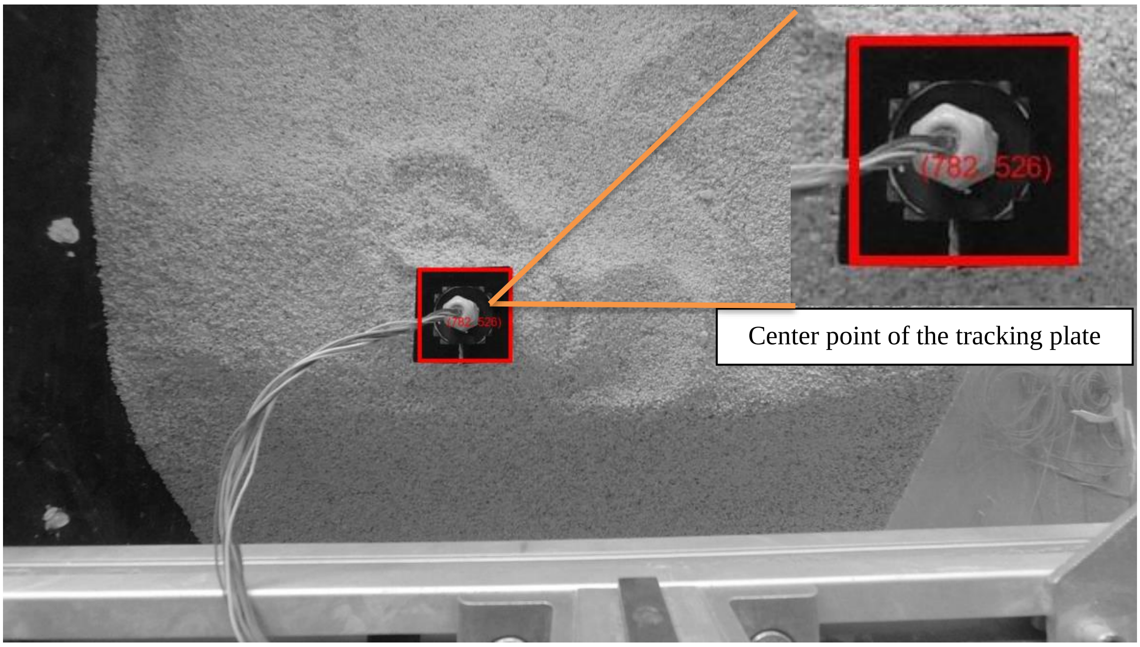

Figure 46. The position of the tracking plate detected by the code

Table 6. Image processing results of Data Set-1

Data Set-1				
	Initial Position (pixels)	Final Position (pixels)	Movement (pixels)	Movement (mm)
Test-1	526	552	26	8,372
Test-2	564	578	14	4,508
Test-3	585	605	20	6,44

5.2. Verification Measurements by Tilt Sensors and Laser Measurements

The instantaneous readings from the tilt sensors placed on the shaking table to verify the image processing data are recorded before the experiment with the help of Witmotion software. Similarly, the distance between the laser measure placed on the measuring apparatus and the top of the pipe where the sensors are placed (also the area where the tracking plate is placed) is measured. Both measurements are made when the shaking table is at rest. Since the camera recording is also started before the movement is triggered, all measurements can be evaluated from the same position.

After the experiment, the recording is switched off after waiting for the camera to record a few more frames at rest. Then, the laser measurements and tilt sensor data are recorded simultaneously. By this way, just as at the beginning of the experiment, the data for the position at the end of the experiment are collected so that they can be compared.

The tilt sensor and laser data are tabulated. The help data calculates how much movement in the tilting pipe corresponds to the angle data measured from the sensors and added to the table. This process is first performed for the lower sensor. A correction must be performed before calculating the upper sensor. In fact, some of the movement in the upper sensor is actually due to the movement in the lower sensor. For this reason, to calculate the movement in the upper part alone, the movement from the lower part should not be included twice. After all these operations, the final analyses of the tilt sensor and laser data for comparison with image processing have been developed and presented in Appendix B. One of the representative examples is given in Table 6**.**

Table 7. Analysis of the entire Data Set-1

Data Set-1							
Test-1			Test-2			Test-3	
Lower Sensor Angle (°)	0,177		Lower Sensor Angle (°)	0,07		Lower Sensor Angle (°)	0,18
Movement (mm)	0,77		Movement (mm)	0,31		Movement (mm)	0,77
Upper Sensor Angle (°)	4,103		Upper Sensor Angle (°)	2,37		Upper Sensor Angle (°)	4,02
Movement (mm)	9,33		Movement (mm)	5,39		Movement (mm)	9,12
Total Movement (mm)	10,10		Total Movement (mm)	5,70		Total Movement (mm)	9,89
Laser Measurement (mm)	12		Laser Measurement (mm)	7		Laser Measurement (mm)	13

6. RESULTS AND DISCUSSION

In this study, the motion of an artificial slope model created on a laboratory-scale shaking table was investigated by various methods. The role of the shaking table in this system was to work as a triggering mechanism by exposing the slope to dynamic effects. Three different measurement methods were used in this system. The first of these was the image processing method. The movement of the tracking plate on the crown of the sliding surface was detected using the image recordings taken with a camera positioned above the experimental setup. The detection of this movement was performed with a code written in Python programming code (Appendix C). The first part of the code breaked a video recording into frames by dividing it into frames. This process aimed to find the instantaneous position of the tracking plate. In the second stage, the frames extracted from the video were converted to grayscale. By this way, it would be easier to distinguish the tracking plate from other objects in the image. As a result of the calibration analyses performed on the sample test images, the RGB values to be considered as the boundary for the plate were determined and defined in the code. In the third stage, the code detected the location of the tracking plate by filtering these boundary values in the image. In the third stage, the code determined each pixel suitable for the boundary RGB values and drawed a square around these pixels. The drawn frame's center point showed the instantaneous position of the plate. The code automatically applied this process for each frame extracted from the video. Thus, position information could be obtained at any time.

With image processing, information can only be obtained on the outer surface. Two tilt sensors were placed in the experimental setup at different depths to get data on the motion projection at lower depths and verify the image processing data. The sensors were placed inside the pipes and printed with a 3D printer in several pieces. Setting the tracking plate used in image processing at the top of these pipes made it possible to make more accurate comparisons by obtaining data from a single object with different methods. The instantaneous slope data from the sensor could be monitored through the Witmotion program. The software also allowed multiple sensors to be operated simultaneously.

In addition to these two methods, laser measurements were made by referencing the top of the tilting pipe, i.e., the sensor cable connection where the tracking plate is located.

After sensor and laser measurements were taken at rest, the slope prepared for testing was subjected to motion within the specified amplitude limits utilizing a shaking table to trigger the movement on the sliding surface. A test was completed when the shaking table completed its motion, and the resultant measurements were taken. The second and third tests were performed with the same measurement procedures without changing the slope and tilting pipe in the resulting position. The sequential tests performed in this way represent a data set. Comparative result data sets showing the image processing, tilt sensor, and laser measurements of the several experiments are shown below. Figures 47, 48 and 49 show the comparative results of three different experiments with the same amplitude.

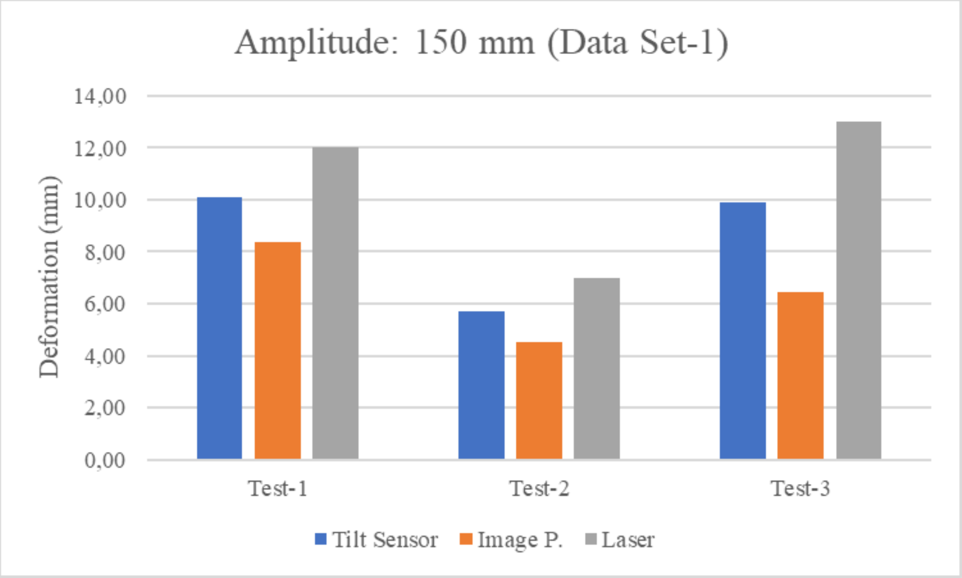

Figure 47. Comparative results of the entire Data Set-1

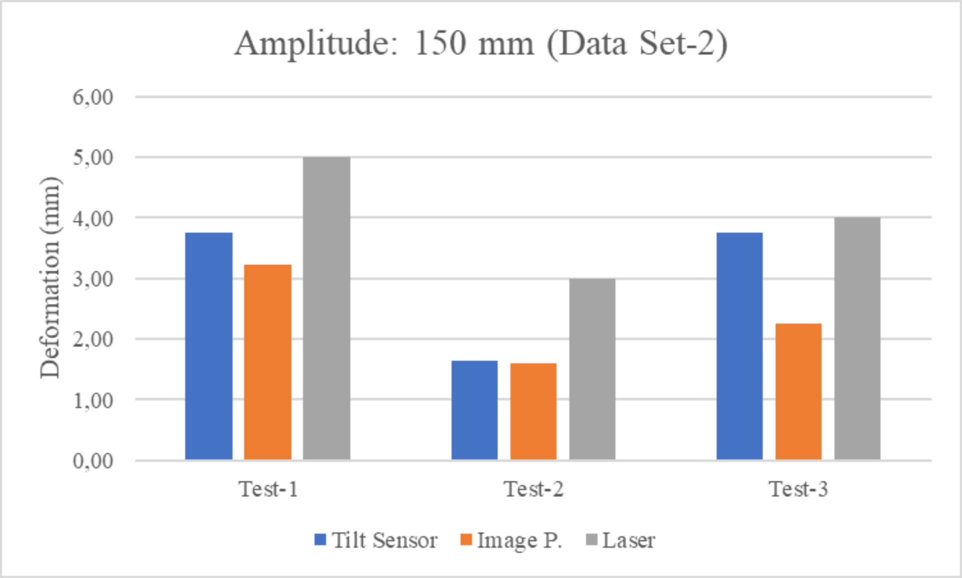

Figure 48. Comparative results of the entire Data Set-2

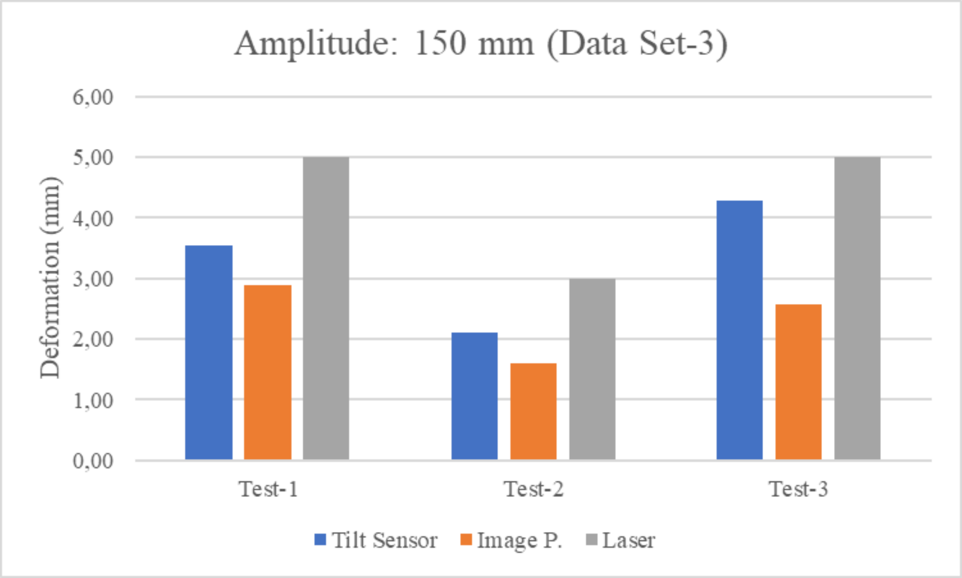

Figure 49. Comparative results of the entire Data Set-3

It is necessary to calculate the progress at the top of the tilting pipe where the sensors are placed to compare the data from the tilt sensor with the image processing results. Since image processing is performed through this region, this process is necessary. Since there were two sensors in the experimental setup, this calculation was done in two steps. The angle value measured by the lower sensor was calculated using the length of the pipe up to the upper sensor connection point. Since the angle value measured by the upper sensor also includes the measurement in the lower sensor, the movement of the tilting pipe in the upper part was calculated by taking the difference between the two values.

The sample data sets show that laser measurement results are larger than image processing and tilt sensor measurements in all graphs. The fact that laser measurements are less precise than other methods led to this result. When looking at the specifications of this product, which gives results in mm on the information screen, it is stated that it has a margin of error of ± 1.5 mm. Experimental results also confirm this information. Nevertheless, laser measurements can be used to get a rough idea on the amount of movement.

When the results were analyzed, it was observed that although the image processing and tilt sensor measurements were close, there were some differences between them. First, the measurement sensitivity conditions must be examined to explain this situation.

Tilt sensors allow measurements with a sensitivity of 0.001 degrees. By this way, motion detection can be performed with an accuracy of approximately 0.01 mm. On the other hand, many factors affect the sensitivity in image processing. The first of these is the distance of the camera to the object to be tracked. The greater the distance between these two objects, the more significant the progress of each pixel will correspond to a greater distance. In other words, the code will need larger movements to see the progress and it implies that the sensitivity is low. Another issue that will affect the sensitivity in image processing is the video resolution. In this study, 1920 x 1080 (Full HD) video recordings were used. While lower resolution options are available, higher resolution options such as 2560 x 1440 (2K) or 3840 x 2160 (4K) were also available. The higher resolution allows smaller distances to be tracked with 1 pixel due to the increased number of pixels. Movement can, therefore, be tracked in smaller steps. In short, high resolution means high sensitivity.

At first, working with the highest possible resolution seems logical, but this option has some problems. As the resolution increases, the file size of the videos increases.

Accordingly, the frames extracted from the video through the code will also be of larger file size. Therefore, more space is needed for file storage. In addition, large-size files will also have an adverse effect on the running time of the code. For these reasons, it is preferred to record in Full HD quality.

As a result of the camera placement and resolution selection, image processing has a measurement accuracy of approximately 0.32 mm. It is one of the reasons for the difference between tilt sensor measurements.

Another reason for the difference between the measurements is that the tracking plate tends to move out of the camera plane as the amount of movement in the pipe increases. Image processing can detect movement in the horizontal plane. As the tilting pipe to which the tracking plate is attached starts to gain angle as the movement in the sand progresses, it varies from the horizontal to the vertical plane. As the movement progresses, the error in the image processing result increases. As the angle of the pipe increases, the portion of the motion that occurs in the vertical plane also increases. This results in a smaller portion of the motion being detected by image processing. For these reasons, the measurements are not exactly equal.

The result data sets given up to this point belonged to the experiments performed with 150 mm amplitude. Tests were performed to examine the effect of amplitude on deformation for 90-130-170 mm amplitude values, and the results are given between Figure 50 and Figure 55.

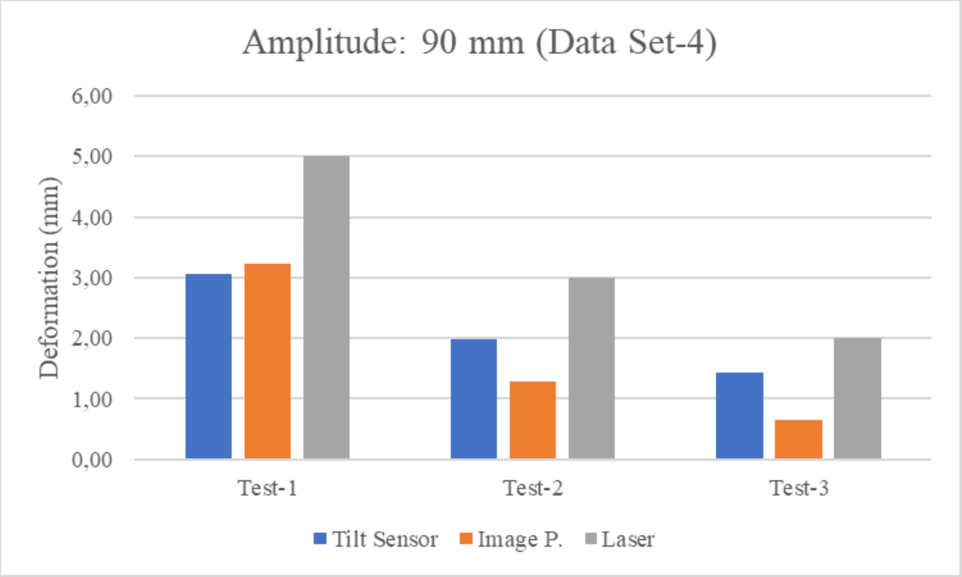

Figure 50. Comparative results of the entire Data Set-4

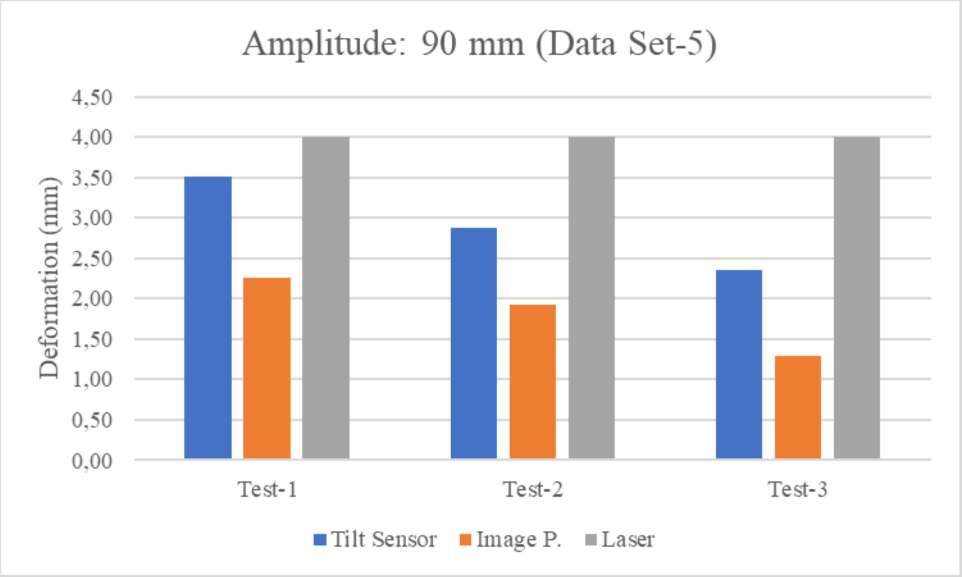

Figure 51. Comparative results of the entire Data Set-5

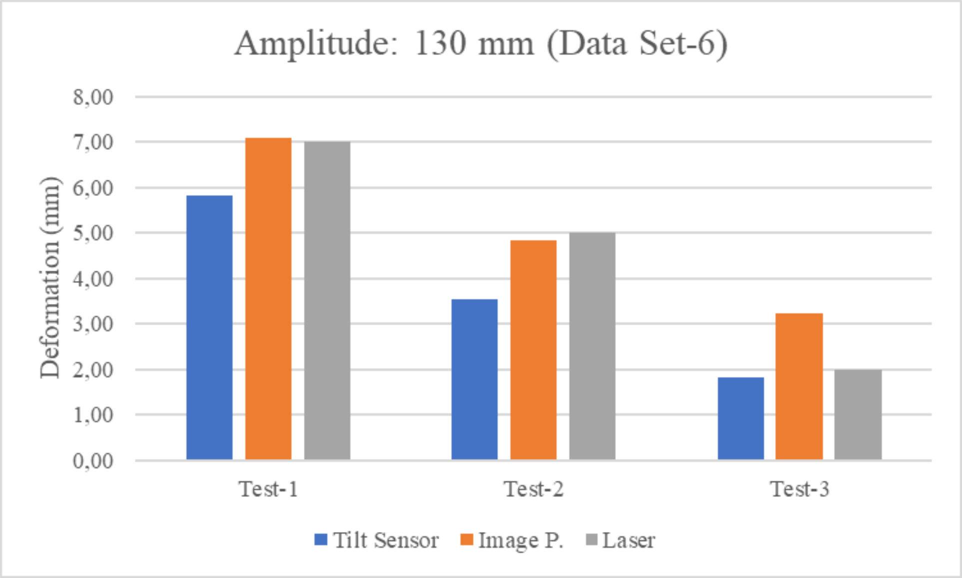

Figure 52. Comparative results of the entire Data Set-6

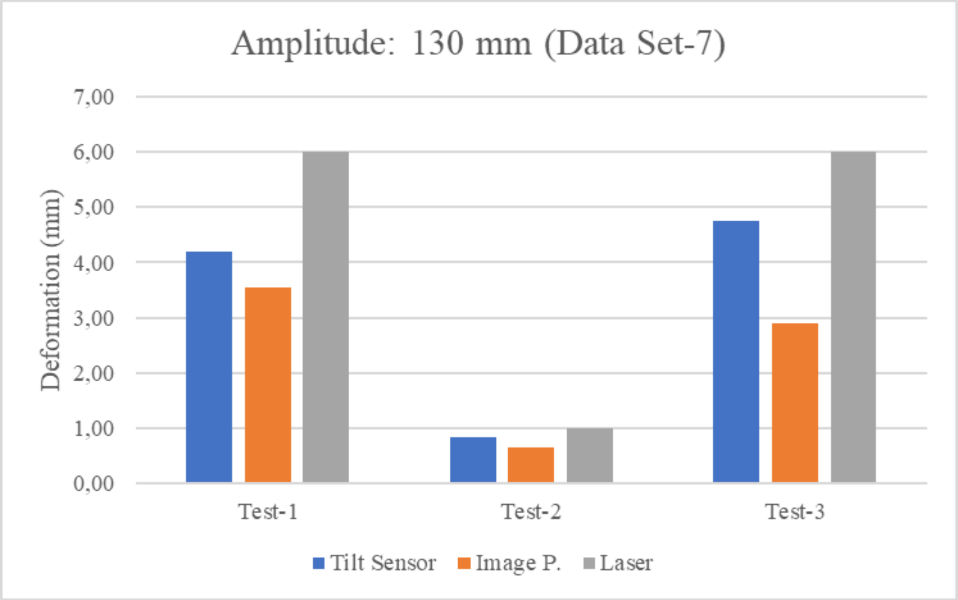

Figure 53. Comparative results of the entire Data Set-7

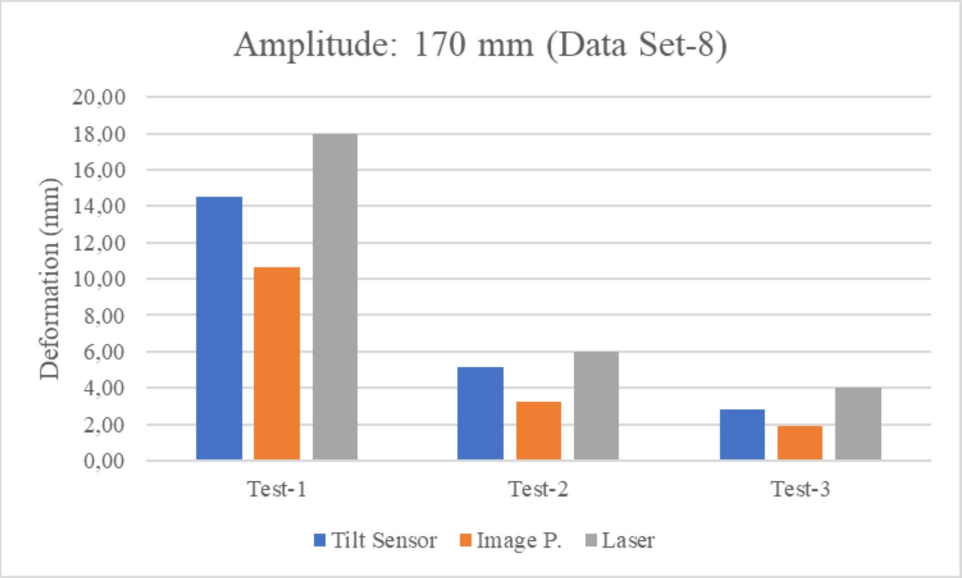

Figure 54. Comparative results of the entire Data Set-8

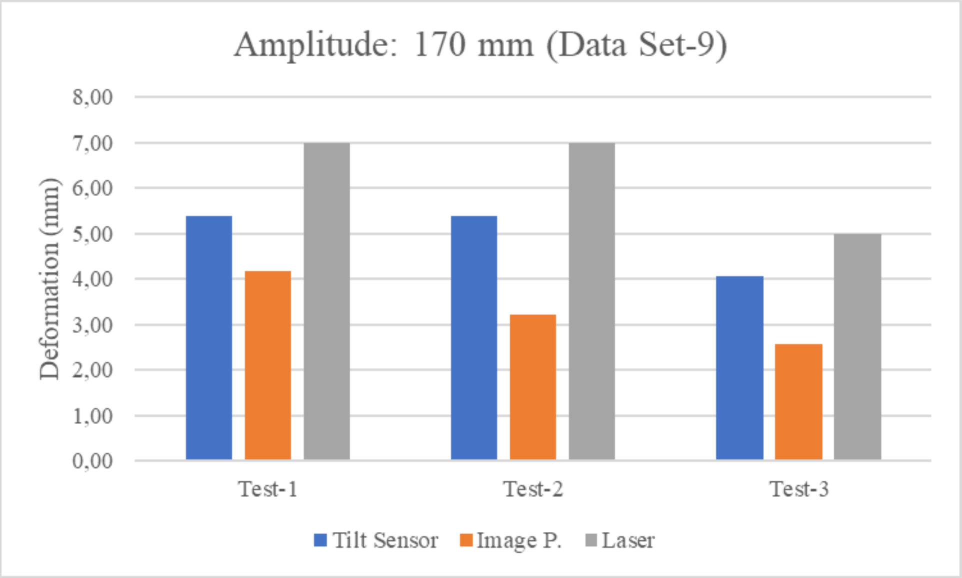

Figure 55. Comparative results of the entire Data Set-9

As a result of these experiments, it was observed that the amplitude is correlated well with the deformation. Although the preparation process of the experiment is based on a standard, it may not always be possible to meet this standard 100% when working with natural materials. However, it can be concluded that as the amplitude increases, the deformation generally increases.

In almost all of the experiments, it was observed that the error rate increased as the number of repeated experiments performed on the same sample increased. As the tilting pipe to which the sensor and the monitoring plate are connected rotates, its movement proceeds vertically rather than horizontally. Therefore, a lesser part of the movement can be detected by image processing.

In addition to the surface monitoring studies, the variation according to depth was also analyzed. For this purpose, the data obtained from the slope sensors correlated with the pipe length and the deformation graphs plotted according to depth. Thus, the projection of the pipes where the sensors are placed is obtained. Note that each graph shows the repetitive experiments performed on a sliding surface (i.e., Test-1, -2, and -3). Finally, these graphs are shown between Figure 56 and 64 for all data sets for which comparative results are given above.

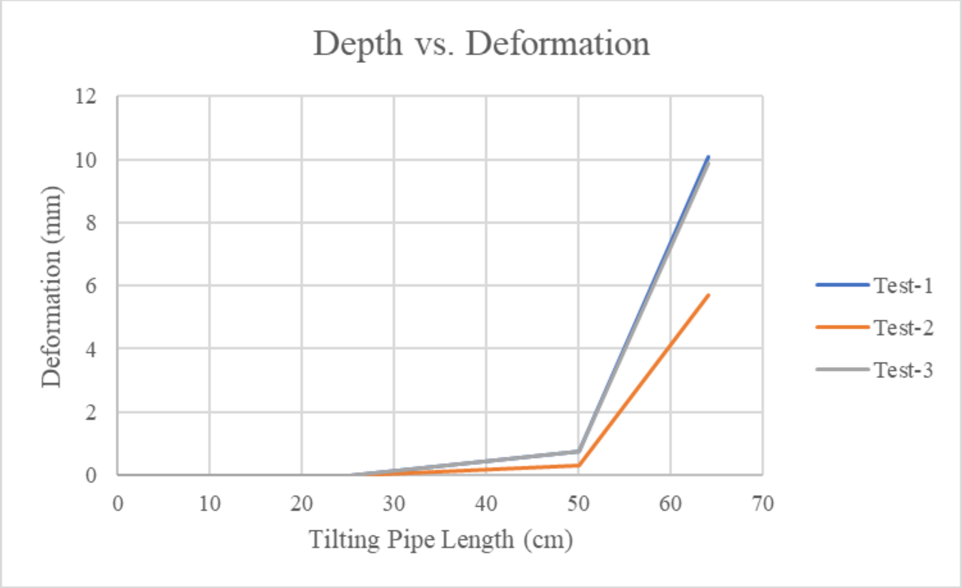

Figure 56. The deformation along the tilting pipe through the depth (Data Set-1)

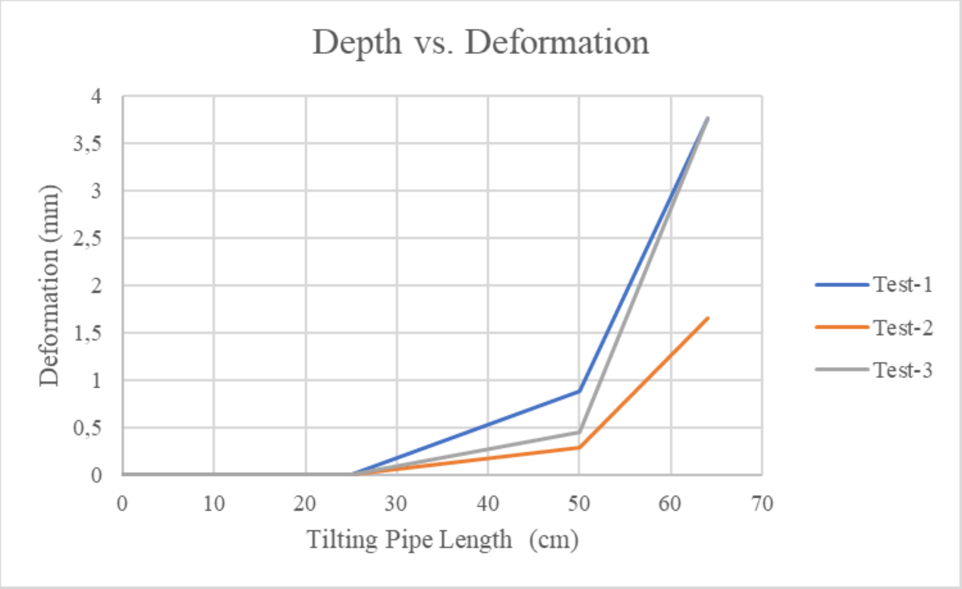

Figure 57. The deformation along the tilting pipe through the depth (Data Set-2)

In the preliminary experiments, there was a problem of fracture of the lower part of the pipe because there was no movement at the base or very close to zero. A piecewise design was used since the high amount of movement in the upper part was impossible in the lower part. Thus, the first 25 centimeters of the tilting pipe was used for fixing, and no deformation measurements were taken. The second section of the pipe between 25-50 centimeters was evaluated according to the bottom sensor data. Above 50 cm, the top section was assessed with the upper sensor data.

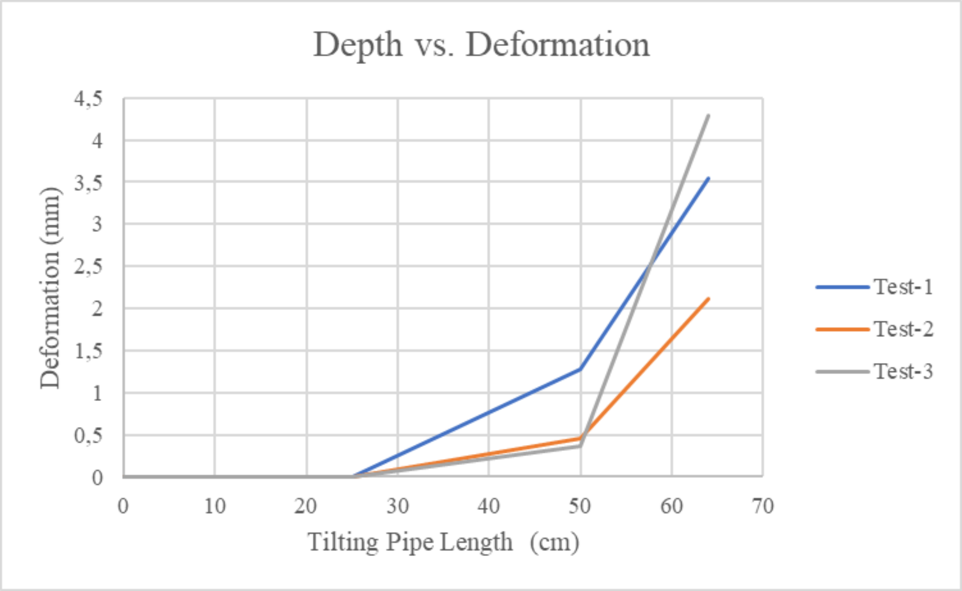

Figure 58. The deformation along the tilting pipe through the depth (Data Set-3)

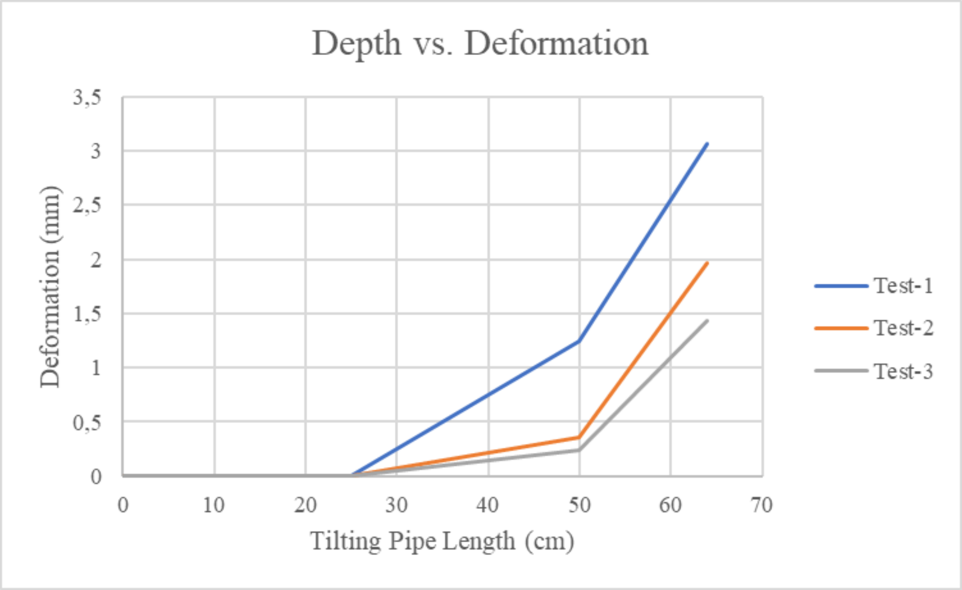

Figure 59. The deformation along the tilting pipe through the depth (Data Set-4)

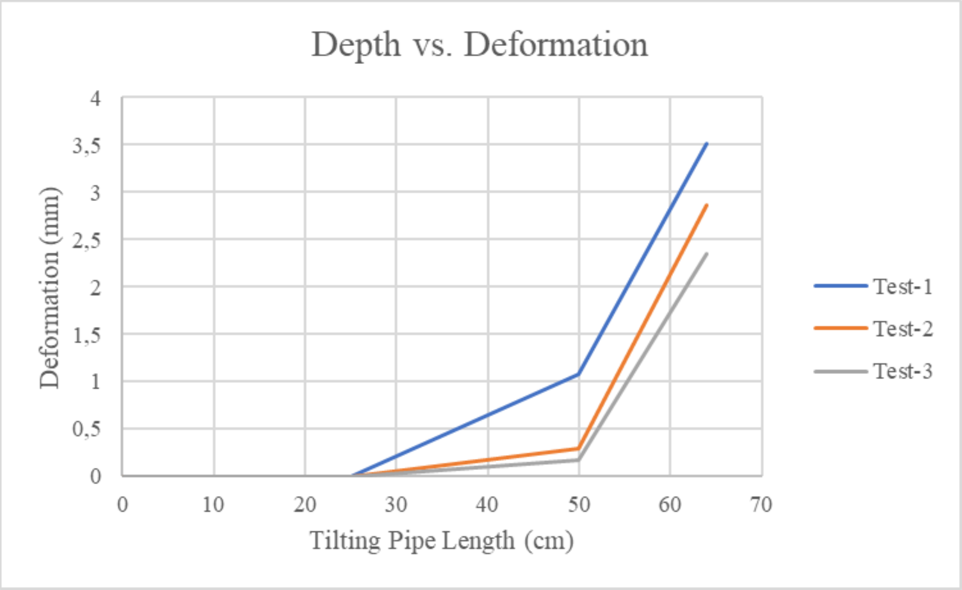

Figure 60. The deformation along the tilting pipe through the depth (Data Set-5)

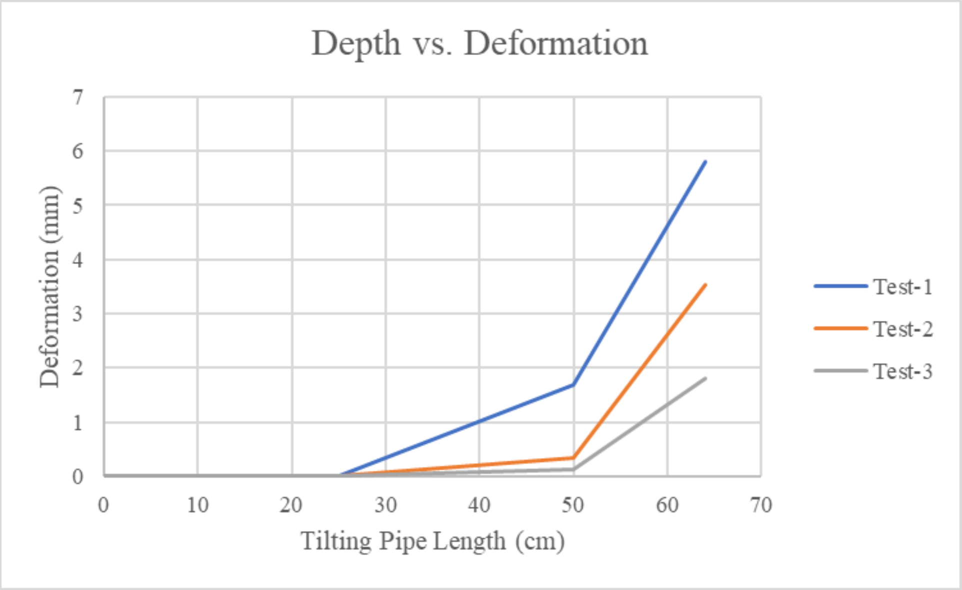

Figure 61. The deformation along the tilting pipe through the depth (Data Set-6)

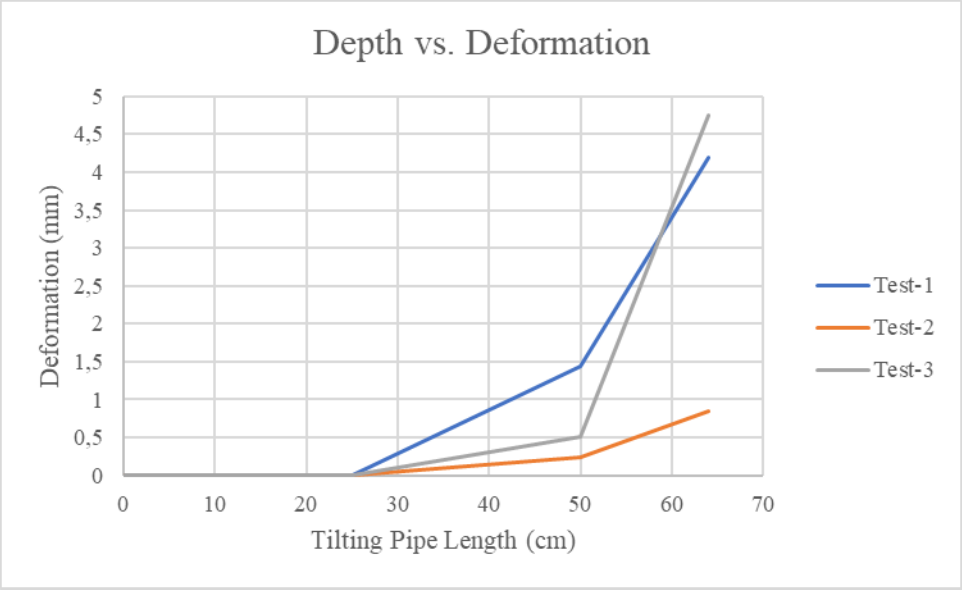

Figure 62. The deformation along the tilting pipe through the depth (Data Set-7)

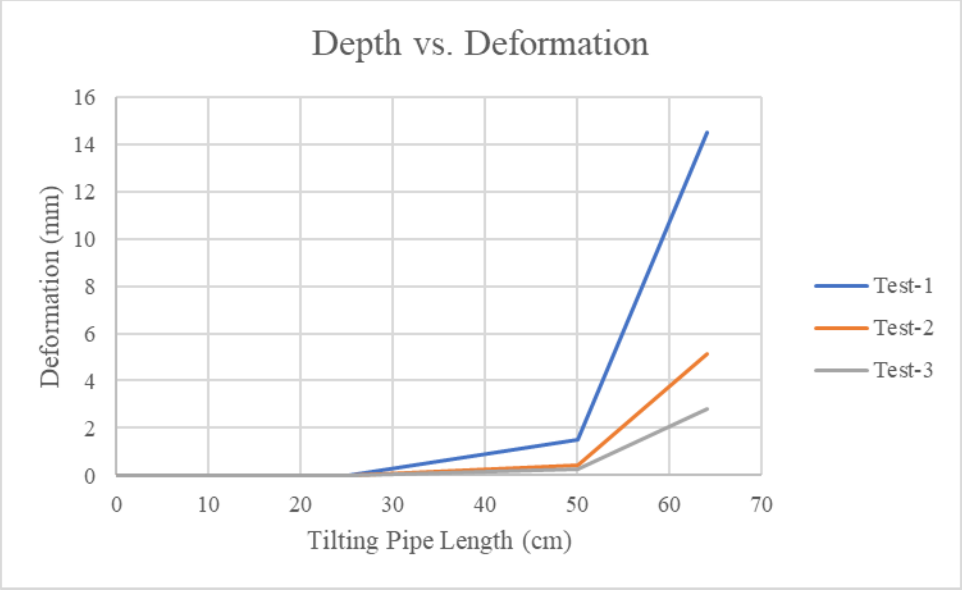

Figure 63. The deformation along the tilting pipe through the depth (Data Set-8)

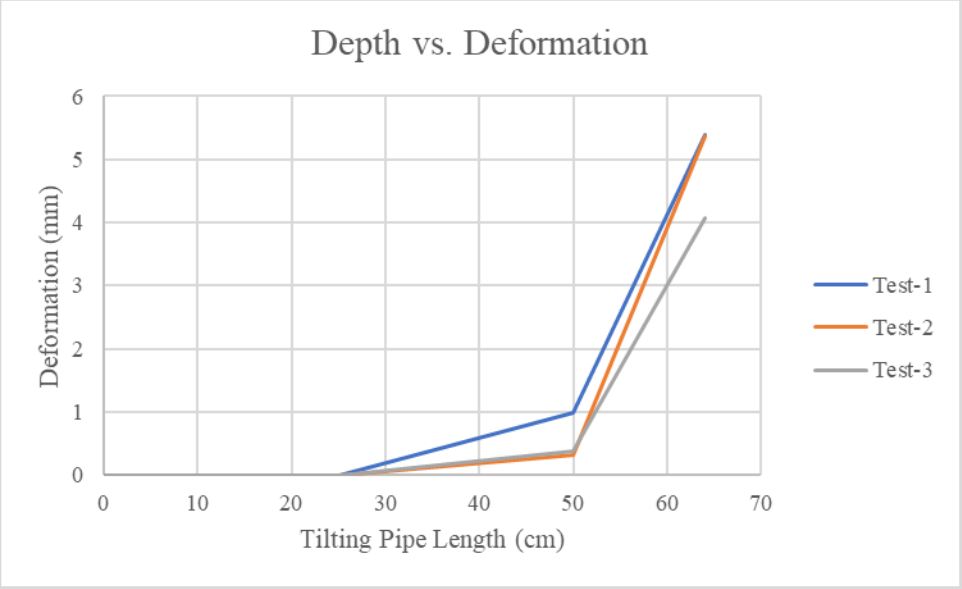

Figure 64. The deformation along the tilting pipe through the depth (Data Set-9)

The results showed that the maximum deformation occurred in the first tests and decreased as the number of tests increased. Most of the deformations occurred in the upper part. The sharp increase in the graphs is related to the number of sensors. As the number of sensors increases, more precise data can be obtained with smoother transitions.

The measurements within the scope of the study were applied by importing a real earthquake acceleration record on the shaking table. This earthquake occurred in 1990 in Los Angeles, California. The results of the experiment are given in Figures 65 and 66.

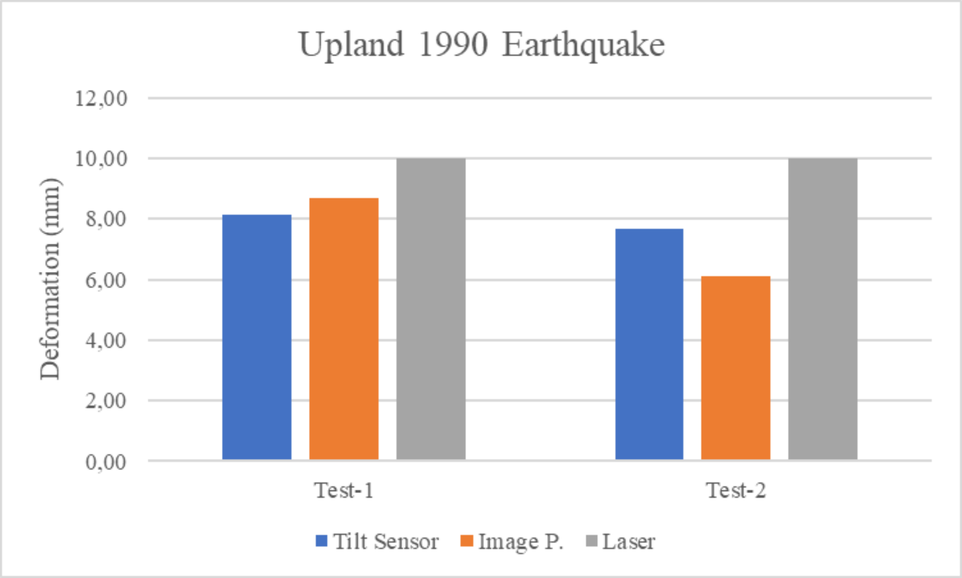

Figure 65. Comparative results of the experiment performed with Upland 1990 earthquake acceleration record

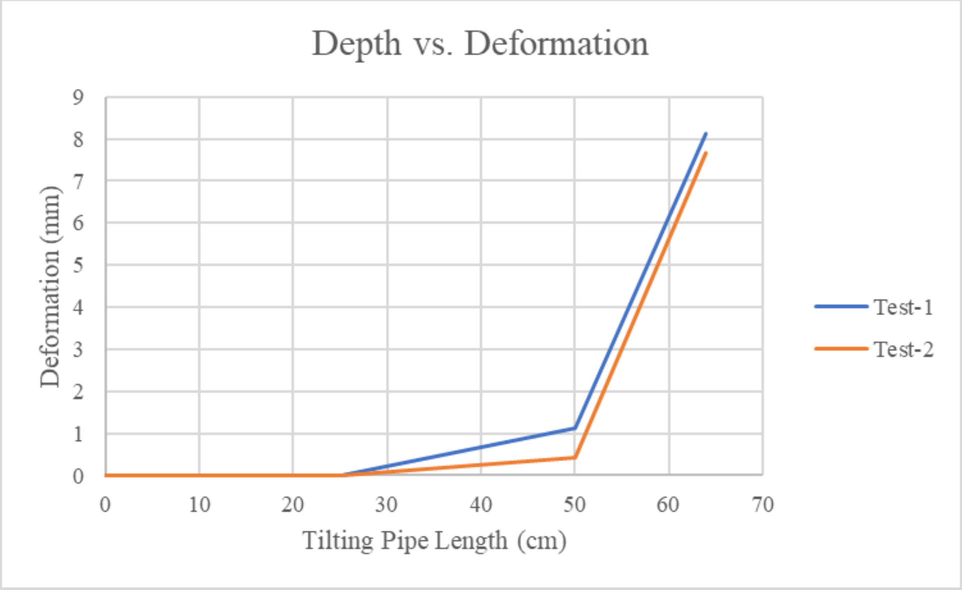

Figure 66. The deformation along the tilting pipe through the depth (considering the Upland 1990 earthquake acceleration record)

7. CONCLUSION AND RECOMMENDATIONS

In this study, a prototype landslide container was built on a shaking table in the laboratory to evaluate mass movements from different perspectives. When the studies on mass movements in the literature are analyzed, image recordings, primarily used in a supporting position, play the leading role in this study. In this context, a high-resolution camera was placed on the upper part of the landslide container, and the experiments were recorded to be analyzed by image processing techniques. A segmented pipe system with two tilt sensors was installed in the container to assess the reliability of the image processing data. In addition, laser measurements were performed on a reference point using an apparatus developed with a 3D printer. A reference plate was also designed and produced with a 3D printer for image processing studies. It is intended to be placed at the top of the pipe where the sensors are placed so that image processing and tilt sensor data can be evaluated from the same point. In this experimental setup, using the shaking table as a triggering mechanism, experiments were carried out using motion records with different amplitudes.

Within the scope of image processing studies, a Python code was written to detect the position of the tracking plate on the image. The code first separated a video into frames. Then, the separated frames were converted into grayscale. By defining the RGB values of the plate to the code, the pixels that meet the RGB value conditions specified by the code were filtered, and a frame was drawn around it. The center of the detected pixels was determined, and its position on the pixel coordinate system was printed on the image. The same process was repeated for each image so that the position of the plate was found for each video frame. The distance traveled was measured in millimeters and recorded using the calibration images for comparison with other measurements.

Consequently, the data obtained from image processing and tilt sensors presented relatively consistent results. However, the reasons for the slight differences between these two measurements were also evaluated. One of the main reasons was that as the tilting pipe continued to rotate, the plate also rotated, so it moved less in the image. Another issue was measurement accuracy. There was no limitation on the sensitivity of the tilt sensor, and it was suitable to work even with very small units. However, to increase the sensitivity in image processing, the number of pixels must be increased, which implied that the resolution must be changed. Higher resolution meant a larger file size and longer processing time on the code. Thus, the requirements should be analyzed correctly, and a balance should be found in the choices. If the number of cameras was increased and the angle at which they were positioned was optimized, the processing area of each camera could be limited, and more precise measurements could be taken. The same consistency could not be achieved in laser measurements. The low sensitivity of the laser device was the main reason for this situation. Such consistency between the two measurements could not be achieved in laser measurements. The low sensitivity of the laser device was the main reason for this situation.

In future studies, researchers can aim to adapt these studies in the laboratory environment to field conditions. It is necessary to conduct studies on camera systems to be placed in the field. Subsequently, code arrangements can be worked on to select a region instead of an object as a reference. Multiple points or regions might be chosen, and the specified regions could be monitored. Long-term records could be taken on pilot regions that were considered to be suspicious regarding stability, and analyses could be performed at desired time intervals after triggering events, such as earthquakes and rainfall. Also, studies could be carried out on integrating satellite images into the system. An interface could be developed for instant data monitoring over live image records. This way, limit values could be determined, and warnings about the detected points could be sent to move above these values. Such an application could serve as an early warning system.

In conclusion, this prototype system was successfully tested from different perspectives in a laboratory environment. Considering the evaluations and observations made within the scope of the study, it is thought that the system is open to improvement by making different inquiries.

8. REFERENCES

- Akgün, H., Koçkar, M. K., Arslan Kelam, A., Kelam, M. A., Eker, A. M. 2017. "Kocaeli İli Heyelan Hareketlerinin İzlenmesinde Fiber Optik Teknolojisinin Kullanımı", UDAPÇ-14-02 Proje Final Raporu.
- Akgün, H., Koçkar, M. K., Arslan Kelam, A., Kelam, M. A., Şentürk, M. D. 2021. "Kocaeli İlinde Heyelan Hareketlerinin Erken Uyarı Sistemleri ile İzlenmesi, Depremle Meydana Gelen Sismik Hareketin ve Diğer Faktörlerin (Hidrojeolojik, Hidrolojik, Yağış koşulları) Heyelan Kütle Hareketlerinde Meydana Gelen Deformasyonlar Üzerindeki Etkilerinin ve Hassasiyetlerinin İncelenmesi", UDAP-Ç-17-04 Proje Final Raporu.
- Alcântara, E., Marengo, J. A., Mantovani, J. R. A., De Resende Londe, L., San, R. L. Y., Park, E., Lin, Y. N., Wang, J., Mendes, T. S. G., Cunha, A. P. M. D. A., Pampuch, L. A., Seluchi, M. E., Simões, S. J. C., Cuartas, L. A., Gonçalves, D. A., Massi, K. G., Alvalá, R. C. D. S., Moraes, O. L. L., De Souza Filho, C. R., . .
- Arslan Kelam, A. A., Akgün, H., & Koçkar, M. K. (3 2022). Application of an optical fiber-based system for mass movement monitoring. Environmental Earth Sciences, Vol. 81. doi:10.1007/s12665-022-10289-w
- Arslan Kelam, A., Kockar, M. K., Akgun, H. 2016. "Utilization of Optical Fiber System for Mass Movement Monitoring," Disaster Science and Engineering, 2(1), 19-24.
- Arslan, A., Kelam, M. A., Eker, A. M., Akgün, H., & Koçkar, M. K. (2015). Optical Fiber Technology to Monitor Slope Movement. In G. Lollino, D. Giordan, G. B. Crosta, J. Corominas, R. Azzam, J. Wasowski, & N. Sciarra (Eds.), Engineering Geology for Society and Territory - Volume 2 (pp. 1425–1429). Cham: Springer International Publishing.
- Atmajati, E. D., Yuliza, E., Habil, H., Sadisun, I. A., Munir, M. M., & Khairurrijal. (2017). A simple landslide model at a laboratory scale. 1857. doi:10.1063/1.4987085
- Barla, G. B., & Paronuzzi, P. (2013). The 1963 Vajont Landslide: 50th anniversary. Rock Mechanics and Rock Engineering, 46(6), 1267–1270. https://doi.org/10.1007/s00603-013-0483-7
- Bek, A., Jeftić, G., Strelec, S., & Jug, J. (2021). Influence of shear rate on the soil's shear strength. Environmental Engineering - Inženjerstvo okoliša, 8(1-2),

39-47. https://doi.org/10.37023/ee.8.1-2.6

- Crean, P., & Buckley, R. (1994). Proceedings of SPIE. https://doi.org/10.1117/12.175315
- Dağ, S., Bulut, F. 2012. “Coğrafi Bilgi Sistemleri Tabanlı Heyelan Duyarlılık Haritalarının Hazırlanmasına Bir Örnek: Çayeli (Rize, KD Türkiye)”, Jeoloji Mühendisliği Dergisi, S:36.
- Fairman, H. S., Brill, M. H., & Hemmendinger, H. (1997). How the CIE 1931 color-matching functions were derived from Wright-Guild data. Color Research and Application, 22(1), 11–23. https://doi.org/10.1002/(sici)1520-6378(199702)22:1
- Fritz, H. M. (2002). PIV applied to landslide generated impulse waves. In Springer eBooks (pp. 305–320). https://doi.org/10.1007/978-3-662-08263-8_18
- Gallage, C., Abeykoon, T., & Uchimura, T. (2 2021). Instrumented model slopes to investigate the effects of slope inclination on rainfall-induced landslides. Soils and Foundations, 61, 160–174. doi:10.1016/j.sandf.2020.11.006
- Geotechdata.info, Angle of Friction, http://geotechdata.info/parameter/angle-of-friction.html (as of September 14.12.2013)
- Gökçe, O., Özden, Ş., Demir, A. 2008. “Türkiye’de Afetlerin Mekansal Ve İstatistiksel Dağılımı Afet Bilgi Envanteri”, T.C. Bayındırlık ve İskan Bakanlığı Afet İşleri Genel Müdürlüğü Afet Etüt ve Hasar Tespit Daire Başkanlığı, Ankara, Türkiye.
- Gürer, İ., & Uçar, I. (2022). The inventory of flood disasters in Turkey. In Environmental earth sciences (pp. 313–322). https://doi.org/10.1007/978-3-031-04375-8_35
- Hojat, A., Arosio, D., Ivanov, V. I., Longoni, L., Papini, M., Scaioni, M., … Zanzi, L. (11 2019). Geoelectrical characterization and monitoring of slopes on a rainfall-triggered landslide simulator. Journal of Applied Geophysics, 170. doi:10.1016/j.jappgeo.2019.103844
- Koenderink, J. J., Van Doorn, A. J., & Gegenfurtner, K. R. (2021). RGB colors and ecological optics. Frontiers in Computer Science, 3. https://doi.org/10.3389/fcomp.2021.630370
- Li, N., & Cheng, Y. M. (2014). 3-D analysis of slope failure mechanism Laboratory and 3-D-distinct element analysis of failure mechanism of slope under external surcharge 3-D analysis of slope failure mechanism. Nat. Hazards Earth

Syst. Sci. Discuss, 2, 5937– 5970. doi:10.5194/nhessd-2-5937-2014

- Lin, M. L., & Wang, K. L. (8 2006). Seismic slope behavior in a large-scale shaking table model test. Engineering Geology, 86, 118–133. doi:10.1016/j.enggeo.2006.02.011
- Lo, C. M., & Weng, M. C. (4 2017). Identification of deformation and failure characteristics in cataclinal slopes using physical modeling. Landslides, 14, 499–515. doi:10.1007/s10346-016-0735-1
- Lü, P., Wu, H., Qiao, G., Li, W., Scaioni, M., Feng, T., Liu, S., Chen, W., Li, N., Liu, C., Tong, X., Hong, Y., & Li, R. (2015). Model test study on monitoring dynamic process of slope failure through spatial sensor network. Environmental Earth Sciences, 74(4), 3315–3332. https://doi.org/10.1007/s12665-015-4369-8
- Montrasio, L., Schilirò, L., & Terrone, A. (2015). Physical and numerical modelling of shallow landslides. Landslides, 13(5), 873–883. https://doi.org/10.1007/s10346-015-0642-x
- Nobre, C. E. (2023). Deadly disasters in southeastern South America: flash floods and landslides of February 2022 in Petrópolis, Rio de Janeiro. Natural Hazards and Earth System Sciences, 23(3), 1157–1175. https://doi.org/10.5194/nhess-23-1157-2023
- Pajalić, S., Peranić, J., Maksimović, S., Čeh, N., Jagodnik, V., & Arbanas, Ž. (2021). Monitoring and data analysis in small-scale landslide physical model. Applied Sciences, 11(11), 5040.
- Pei, H., Cui, P., Yin, J., Zhu, H., Chen, X., Pei, L., & Xu, D. (10 2011). Monitoring and warning of landslides and debris flows using an optical fiber sensor technology. Journal of Mountain Science, 8, 728–738. doi:10.1007/s11629-011-2038-2
- Rory, C. (2014). Comandante: Hugo Chavez's Venezuela. Penguin Books: New York. (pp. 44–46). ISBN 978-0143124887.
- Savvaidis, P. D. (2003). Existing landslide monitoring systems and techniques. From stars to earth and culture, 242-258.
- Sim, K. B., Lee, M. L., & Wong, S. Y. (2022b). A review of landslide acceptable risk and tolerable risk. Geoenvironmental Disasters, 9(1). https://doi.org/10.1186/s40677-022-00205-6
- Sugiarto, K., Kusuma, V. A., Firdaus, A. A., Suprapto, S. S., & Putra, D. F. U. (2023). Implementing hue-saturation-value filter and circle hough transform for

object tracking on ball-wheeled robot. International Journal of Reconfigurable & Embedded Systems (IJRES), 13(1), 52. https://doi.org/10.11591/ijres.v13.i1.pp52-58

- Topaçli, Z. K., Ozcan, A. K., & Gökçeoğlu, C. (2023). Performance Comparison of Landslide Susceptibility Maps Derived from Logistic Regression and Random Forest Models in the Bolaman Basin, Türkiye. Natural Hazards Review, 25(1). https://doi.org/10.1061/nhrefo.nheng-1771
- Wang, B., HouHengjun, & ZhuZhengwei. (2021). Transparency and applications of transparent soil: a review. Geotechnical Research, 8(4), 130–138. https://doi.org/10.1680/jgere.21.00016
- Wartman, J., Seed, R. B., Bray, J. D. 2005. "Shaking Table Modeling of Seismically Induced Deformations in Slopes," Journal of Geotechnical and Geoenvironmental Eng., 131(5): 610-622.
- White, D. J., Take, W. A., & Bolton, M. D. (2001). Measuring soil deformation in geotechnical models using digital images and PIV analysis. 10th International Conference on Computer Methods and Advances in Geomechanics. Tucson, Arizona. Pp 997-1002 Pub. Balkema, Rotterdam., 997–1002. http://publications.eng.cam.ac.uk/329001/
- Witmotion. (2023). Witmotion GitHub Repositories. last accessed 27 December 2023 "<https://github.com/WITMOTION?tab=repositories>"
- Yin, J., Liu, J., Fan, K., & Wang, S. (2023). Integrating image processing and deep learning for effective analysis and classification of dust pollution in mining processes. International Journal of Coal Science & Technology, 10(1). https://doi.org/10.1007/s40789-023-00653-x
- Yuan B, Xiong L, Zhai L, Zhou Y, Chen G, Gong X and Zhang W (2019) Transparent Synthetic Soil and Its Application in Modeling of Soil-Structure Interaction Using Optical System. Front. Earth Sci. 7:276. doi: 10.3389/feart.2019.00276
- Zelazko, A. (2023, November 10). RGB color model. Encyclopedia Britannica. https://www.britannica.com/science/RGB-color-model
- Zhang, C., Fu, G., Lai, Z., Du, X., Wang, P., Dong, H., & Jia, H. (2020). Shake table test of long-span cable-stayed bridge subjected to near-fault ground motions considering velocity pulse effect and non-uniform excitation. Applied Sciences, 10(19), 6969. 9

- Zhang, G., Liang, D., & Zhang, J. (2006). Image analysis measurement of soil particle movement during a soil–structure interface test. Computers and Geotechnics, 33(4–5), 248–259. https://doi.org/10.1016/j.compgeo.2006.05.003
- Zhang, Y., Zhang, X., Zhang, S., Yang, Y., Du, X., Li, Z., & Zhang, Y. (2023). Research on Eccentric Cavitation Bubble Collapse Dynamics within Droplets. Symmetry, 15(7), 1375. https://doi.org/10.3390/sym15071375Kundu, R. (2023, April 20). Image Processing: Techniques, Types, & Applications (2023). V7. https://www.v7labs.com/blog/image-processing-guide
- Zhao, M., Huang, D., Cao, M., & Qiao, J. (2015). 520. Shaking table tests on deformation and failure mechanisms of the seismic slope. 17.
- Zhou, J., Xu, F., & Guo, C. (2016). Effects of model parameters, topography, and scale on the mass movement processes of debris avalanches using the discrete element method. Arabian Journal of Geosciences, 9(5). https://doi.org/10.1007/s12517-016-2441-7

APPENDICES

APPENDIX A – Image Processing Results for all Data Sets

Table A1. Image processing results of Data Set-1

Data Set-1				
	Initial Position (pixels)	Final Position (pixels)	Movement (pixels)	Movement (mm)
Test-1	526	552	26	8,372
Test-2	564	578	14	4,508
Test-3	585	605	20	6,44

Table A2. Image processing results of Data Set-2

Data Set-2				
	Initial Position (pixels)	Final Position (pixels)	Movement (pixels)	Movement (mm)
Test-1	528	538	10	3,22
Test-2	543	548	5	1,61
Test-3	550	557	7	2,254

Table A3. Image processing results of Data Set-3

Data Set-3				
	Initial Position (pixels)	Final Position (pixels)	Movement (pixels)	Movement (mm)
Test-1	530	539	9	2,898
Test-2	544	549	5	1,61
Test-3	552	560	8	2,576

Table A4. Image processing results of Data Set-4

Data Set-4				
	Initial Position (pixels)	Final Position (pixels)	Movement (pixels)	Movement (mm)
Test-1	536	546	10	3,22
Test-2	548	552	4	1,288
Test-3	556	558	2	0,644

Table A5. Image processing results of Data Set-5

Data Set-5				
	Initial Position (pixels)	Final Position (pixels)	Movement (pixels)	Movement (mm)
Test-1	542	549	7	2,254
Test-2	553	559	6	1,932
Test-3	563	567	4	1,288

Table A6. Image processing results of Data Set-6

Data Set-6				
	Initial Position (pixels)	Final Position (pixels)	Movement (pixels)	Movement (mm)
Test-1	541	559	18	5,796
Test-2	565	574	9	2,898
Test-3	578	583	5	1,61

Table A7. Image processing results of Data Set-7

Data Set-7				
	Initial Position (pixels)	Final Position (pixels)	Movement (pixels)	Movement (mm)
Test-1	528	539	11	3,542
Test-2	547	549	2	0,644
Test-3	550	559	9	2,898

Table A8. Image processing results of Data Set-8

Data Set-8				
	Initial Position (pixels)	Final Position (pixels)	Movement (pixels)	Movement (mm)
Test-1	535	568	33	10,626
Test-2	590	600	10	3,22
Test-3	609	615	6	1,932

Table A9. Image processing results of Data Set-9

Data Set-9				
	Initial Position (pixels)	Final Position (pixels)	Movement (pixels)	Movement (mm)
Test-1	531	544	13	4,186
Test-2	554	564	10	3,22
Test-3	575	583	8	2,576

Table A10. Image processing results of the experiment performed with Upland 1990 earthquake acceleration record

Upland 1990 Earthquake				
	Initial Position (pixels)	Final Position (pixels)	Movement (pixels)	Movement (mm)
Test-1	519	546	27	8,694
Test-2	555	574	19	6,118

APPENDIX B – Tilt Sensor and Laser Measurements for all Data Sets

Table B1. Tilt Sensor and Laser Measurements of Data Set-1

Data Set-1							
Test-1			Test-2			Test-3	
Lower Sensor Angle (°)	0,177		Lower Sensor Angle (°)	0,07		Lower Sensor Angle (°)	0,18
Movement (mm)	0,77		Movement (mm)	0,31		Movement (mm)	0,77
Upper Sensor Angle (°)	4,103		Upper Sensor Angle (°)	2,37		Upper Sensor Angle (°)	4,02
Movement (mm)	9,33		Movement (mm)	5,39		Movement (mm)	9,12
Total Movement (mm)	10,10		Total Movement (mm)	5,70		Total Movement (mm)	9,89
Laser Measurement (mm)	12		Laser Measurement (mm)	7		Laser Measurement (mm)	13

Table B2. Tilt Sensor and Laser Measurements of Data Set-2

Data Set-2							
Test-1			Test-2			Test-3	
Lower Sensor Angle (°)	0,202		Lower Sensor Angle (°)	0,07		Lower Sensor Angle (°)	0,1
Movement (mm)	0,88		Movement (mm)	0,29		Movement (mm)	0,45
Upper Sensor Angle (°)	1,269		Upper Sensor Angle (°)	0,6		Upper Sensor Angle (°)	1,46
Movement (mm)	2,88		Movement (mm)	1,36		Movement (mm)	3,30
Total Movement (mm)	3,76		Total Movement (mm)	1,65		Total Movement (mm)	3,76
Laser Measurement (mm)	5		Laser Measurement (mm)	3		Laser Measurement (mm)	4

Table B3. Tilt Sensor and Laser Measurements of Data Set-3

Data Set-3							
Test-1			Test-2			Test-3	
Lower Sensor Angle (°)	0,291		Lower Sensor Angle (°)	0,11		Lower Sensor Angle (°)	0,08
Movement (mm)	1,27		Movement (mm)	0,46		Movement (mm)	0,36
Upper Sensor Angle (°)	1,005		Upper Sensor Angle (°)	0,73		Upper Sensor Angle (°)	1,73
Movement (mm)	2,28		Movement (mm)	1,66		Movement (mm)	3,93
Total Movement (mm)	3,55		Total Movement (mm)	2,12		Total Movement (mm)	4,28
Laser Measurement (mm)	5		Laser Measurement (mm)	3		Laser Measurement (mm)	5

Table B4. Tilt Sensor and Laser Measurements of Data Set-4

Data Set-4					
Test-1		Test-2		Test-3	
Lower Sensor Angle (°)	0,285	Lower Sensor Angle (°)	0,08	Lower Sensor Angle (°)	0,05
Movement (mm)	1,24	Movement (mm)	0,36	Movement (mm)	0,24
Upper Sensor Angle (°)	0,802	Upper Sensor Angle (°)	0,71	Upper Sensor Angle (°)	0,53
Movement (mm)	1,82	Movement (mm)	1,61	Movement (mm)	1,20
Total Movement (mm)	3,06	Total Movement (mm)	1,97	Total Movement (mm)	1,44
Laser Measurement (mm)	5	Laser Measurement (mm)	3	Laser Measurement (mm)	2

Table B5. Tilt Sensor and Laser Measurements of Data Set-5

Data Set-5					
Test-1		Test-2		Test-3	
Lower Sensor Angle (°)	0,25	Lower Sensor Angle (°)	0,07	Lower Sensor Angle (°)	0,04
Movement (mm)	1,08	Movement (mm)	0,29	Movement (mm)	0,17
Upper Sensor Angle (°)	1,07	Upper Sensor Angle (°)	1,14	Upper Sensor Angle (°)	0,96
Movement (mm)	2,43	Movement (mm)	2,58	Movement (mm)	2,18
Total Movement (mm)	3,51	Total Movement (mm)	2,87	Total Movement (mm)	2,35
Laser Measurement (mm)	4	Laser Measurement (mm)	4	Laser Measurement (mm)	4

Table B6. Tilt Sensor and Laser Measurements of Data Set-6

Data Set-6					
Test-1		Test-2		Test-3	
Lower Sensor Angle (°)	0,38	Lower Sensor Angle (°)	0,08	Lower Sensor Angle (°)	0,03
Movement (mm)	1,68	Movement (mm)	0,34	Movement (mm)	0,12
Upper Sensor Angle (°)	1,82	Upper Sensor Angle (°)	1,41	Upper Sensor Angle (°)	0,75
Movement (mm)	4,14	Movement (mm)	3,19	Movement (mm)	1,69
Total Movement (mm)	5,82	Total Movement (mm)	3,53	Total Movement (mm)	1,82
Laser Measurement (mm)	7	Laser Measurement (mm)	5	Laser Measurement (mm)	2

Table B7. Tilt Sensor and Laser Measurements of Data Set-7

Data Set-7							
Test-1			Test-2			Test-3	
Lower Sensor Angle (°)	0,33		Lower Sensor Angle (°)	0,05		Lower Sensor Angle (°)	0,12
Movement (mm)	1,44		Movement (mm)	0,24		Movement (mm)	0,51
Upper Sensor Angle (°)	1,214		Upper Sensor Angle (°)	0,27		Upper Sensor Angle (°)	1,87
Movement (mm)	2,75		Movement (mm)	0,61		Movement (mm)	4,24
Total Movement (mm)	4,19		Total Movement (mm)	0,85		Total Movement (mm)	4,75
Laser Measurement (mm)	6		Laser Measurement (mm)	1		Laser Measurement (mm)	6

Table B8. Tilt Sensor and Laser Measurements of Data Set-8

Data Set-8							
Test-1			Test-2			Test-3	
Lower Sensor Angle (°)	0,351		Lower Sensor Angle (°)	0,09		Lower Sensor Angle (°)	0,06
Movement (mm)	1,53		Movement (mm)	0,41		Movement (mm)	0,26
Upper Sensor Angle (°)	5,691		Upper Sensor Angle (°)	2,09		Upper Sensor Angle (°)	1,13
Movement (mm)	12,96		Movement (mm)	4,75		Movement (mm)	2,56
Total Movement (mm)	14,49		Total Movement (mm)	5,16		Total Movement (mm)	2,82
Laser Measurement (mm)	18		Laser Measurement (mm)	6		Laser Measurement (mm)	4

Table B9. Tilt Sensor and Laser Measurements of Data Set-9

Data Set-9							
Test-1			Test-2			Test-3	
Lower Sensor Angle (°)	0,23		Lower Sensor Angle (°)	0,07		Lower Sensor Angle (°)	0,09
Movement (mm)	0,98		Movement (mm)	0,31		Movement (mm)	0,38
Upper Sensor Angle (°)	1,95		Upper Sensor Angle (°)	2,23		Upper Sensor Angle (°)	1,62
Movement (mm)	4,41		Movement (mm)	5,06		Movement (mm)	3,68
Total Movement (mm)	5,40		Total Movement (mm)	5,38		Total Movement (mm)	4,06
Laser Measurement (mm)	7		Laser Measurement (mm)	7		Laser Measurement (mm)	5

Table B10. Tilt Sensor and Laser Measurements of the experiment performed with Upland 1990 earthquake acceleration record

Upland 1990 Earthquake				
Test-1			Test-2	
Lower Sensor Angle (°)	0,258		Lower Sensor Angle (°)	0,1
Movement (mm)	1,13		Movement (mm)	0,43
Upper Sensor Angle (°)	3,082		Upper Sensor Angle (°)	3,18
Movement (mm)	7,00		Movement (mm)	7,22
Total Movement (mm)	8,13		Total Movement (mm)	7,65
Laser Measurement (mm)	10		Laser Measurement (mm)	10

APPENDIX C – Python Code for Image Processing Operations

```
import os
from PIL import Image, ImageDraw, ImageFont
import statistics
import cv2
import numpy as np
import matplotlib.pyplot as plt

video_path = 'DJI_0564.MP4'

output_dir = 'extracted_frames_564'
os.makedirs(output_dir, exist_ok=True)

cap = cv2.VideoCapture(video_path)

frame_count = 0

while True:

    ret, frame = cap.read()

    if not ret:
        break

    frame_filename = os.path.join(output_dir, f'frame_enes{frame_count:04d}.jpg')
    cv2.imwrite(frame_filename, frame)
```

```
    frame_count += 1

    print(f"Extracted frame {frame_count}")

cap.release()

print("Frame extraction completed.")

def img2gray(img):
    gray = np.dot(img[..., :3], [0.299, 0.587, 0.114])
    return gray

def process_images(input_folder, output_folder):
    file_list = os.listdir(input_folder)

    os.makedirs(output_folder, exist_ok=True)

    for file_name in file_list:

        input_path = os.path.join(input_folder, file_name)

        base_name, ext = os.path.splitext(file_name)

        image = plt.imread(input_path)
```

```
        gray_image = img2gray(image)

        output_path = os.path.join(output_folder, base_name + '_grayscale' + ext)

        plt.imsave(output_path, gray_image, cmap='gray')

input_folder = 'extracted_frames_564'
output_folder = 'gs_564'

process_images(input_folder, output_folder)


x_values = []
y_values = []

def draw_circle(image, x, y, radius):
    draw = ImageDraw.Draw(image)
    draw.ellipse((x - radius, y - radius, x + radius, y + radius), outline="red")

def draw_rectangle(image, x, y, width):
    draw = ImageDraw.Draw(image)
    draw.rectangle((x - width, y - width, x + width, y + width), outline="red", width=7)

def draw_text(image, x, y, text, font_size=20):
    font = ImageFont.load_default()
```

```
    draw = ImageDraw.Draw(image)
    draw.text((x-30, y), text, fill="red", font=ImageFont.truetype("arial.ttf", font_size))



def process_image(input_path, output_path):
    image = Image.open(input_path)

    global min_x, max_x, min_y, max_y

    for x in range(650, 900):
        for y in range(0, 800):
            r, _, _ = image.getpixel((x, y))
            if r < 50:
                x_values.append(x)
                y_values.append(y)

    center_x = statistics.mean(x_values)
    center_y = statistics.mean(y_values)
    draw_rectangle(image, center_x, center_y, width=80)

    label_text = f"({round(center_x)}, {round(center_y)})"
    draw_text(image, center_x, center_y, label_text)

    image.save(output_path)

if __name__ == "__main__":
```

```
input_directory = "gs_564"
output_directory = "modified_frames_564"
os.makedirs(output_directory, exist_ok=True)

process_every_n_images = 10

processed_count = 0

file_list = sorted(os.listdir(input_directory))
num_files = len(file_list)

for i, filename in enumerate(file_list):
    if filename.endswith(".jpg"):
        if i < 10 or i >= num_files - 10 or (i - 10) % process_every_n_images == 0:
            input_path = os.path.join(input_directory, filename)
            output_path = os.path.join(output_directory, filename)
            process_image(input_path, output_path
```